Existence and stability chart for the ac-driven, damped nonlinear Schrödinger solitons

I. V. Barashenkov* and Yu. S. Smirnov†
Department of Applied Mathematics, University of Cape Town, Private Bag Rondebosch 7700, Western Cape, South Africa
(Received 19 March 1996; revised manuscript received 3 July 1996)

We study the externally driven damped nonlinear Schrödinger equation on an infinite line. The existence and stability chart for its soliton solution is constructed on the plane of two control parameters: the forcing amplitude h and the dissipation coefficient γ. For generic values of h and γ there are two coexisting solitons, one of which (ψ_+) is always unstable. The bifurcation diagram of the second soliton (ψ_-) depends on the dissipation coefficient: if $\gamma<\gamma_{\rm cr}$, the ψ_- is stable for small h and loses its stability via a Hopf bifurcation as h is increased; if $\gamma>\gamma_{\rm cr}$, the ψ_- is stable for all h. There are no ''stability windows'' in the unstable region. We show that the previously reported stability windows occur only when the equation is considered on a finite (and small) spatial interval. [S1063-651X(96)07210-8]

PACS number(s): 03.40.Kf, 05.45.+b, 75.30.Ds

I. INTRODUCTION

A. Motivation

In the past 15 years the role of low-dimensional spatially localized attractors in the nonlinear partial differential equations has been widely appreciated and a great depth of understanding of their properties achieved. Especially well documented are the ac-driven damped sine-Gordon system

$$q_{\tau\tau}-q_{zz}+\sin q=-\alpha q_\tau+\Gamma\sin(\omega\tau) \tag{1}$$

and its small-amplitude limit, the externally driven damped nonlinear Schrödinger equation (NLS)

$$i\Psi_t+\Psi_{xx}+2|\Psi|^2\Psi=-i\gamma\Psi-he^{i\Omega t}. \tag{2}$$

Both systems have numerous applications in a variety of fields, including long Josephson junctions, easy-axis ferromagnets in microwave fields, and a rf-driven plasma.

An initial step in the analysis of the damped driven NLS solitons was made by Kaup and Newell [1]. Under the assumption that the damping and driving are weak, these authors developed an inverse scattering-based adiabatic perturbation procedure to realize that solitons lock to the frequency of the driver. For small h and γ, there are two coexisting phase-locked solitons, one corresponding to focus and the other one to saddle of Kaup and Newell's adiabatic equations (i.e., one soliton is stable and the other one unstable against adiabatic perturbations of their amplitude and phase). This result remains valid for the sine-Gordon breather, whose small-amplitude counterpart is the NLS soliton [2].

Subsequent computer simulations of Eqs. (1) and (2) revealed a rich variety of spatially coherent attractors, including temporally periodic and chaotic states [3–5]. A particularly important observation was that even in chaotic regimes, the spatial structure of the field can be relatively simple and described by only a few spatially localized solitonic modes. A special role of the soliton (or soliton wave train if periodic boundary conditions are implied) has therefore been reinforced for the damped driven systems.

The bifurcations and routes to chaos in the dynamics of a single soliton were studied both numerically and analytically, mainly within perturbative and variational approaches [6–13]. One of the main difficulties here is that soliton solutions are not available in closed form. (Here by soliton we mean the NLS soliton, the sine-Gordon breather, and their wave train counterparts.) Particularly relevant for the present work is Ref. [9], where the spectrum of linearized excitations was studied in order to understand the soliton's instability mechanism. Although providing an important qualitative insight into the dynamics of eigenvalues on the complex plane, the conclusions of [9] were based on a heuristic ansatz for the solution (the phase was assumed to be constant) and had to be verified using the numerically found soliton profiles [15].

In the undamped case ($\gamma=0$) the two coexisting soliton solutions can be found explicitly; the stability problem is also more amenable to analytical study in this case. In particular, one can prove that one of the solitons is unstable *for all* h, not necessarily small ones. As far as the second soliton is concerned, it can lose its stability only via a Hopf bifurcation [14].

Terrones, McLaughlin, Overman, and Pearlstein considered the full damped driven NLS equation on a finite interval [15]. They constructed x-periodic solutions perturbatively, as power series over small parameter multiplying the driver's strength and dissipation coefficient; also they have computed these solutions numerically. For small values of h and γ two soliton wave trains were recovered corresponding to the saddle and focus of Kaup and Newell's adiabatic equations. In Ref. [15] the spatial period was linked to the value of the dissipation coefficient; more precisely, Terrones *et al.* took $L=15.18$ for $\gamma=0.1000$, $L=13.15$ for $\gamma=0.1333$, $L=12.24$ for $\gamma=0.1538$, and $L=10.73$ for $\gamma=0.2000$. For these values of L and γ they solved numerically the linearized eigenvalue problem and demonstrated the existence of the Hopf bifurcation.

An interesting phenomenon encountered in Ref. [15] was the *stability windows*. Increasing the driver's strength for the fixed dissipation coefficient, the eigenvalue of the linearized

*Electronic address: igor@uctvms.uct.ac.za
†Electronic address: smirnov@maths.uct.ac.za

operator crosses the imaginary axis into the right half of the complex plane (unstable region), then returns to the left half, and then crosses into the unstable region again. There are *three* Hopf bifurcations, therefore, and there is a certain region where the spatially periodic solution regains its stability.

In this paper we consider localized solutions of Eq. (2) on the infinite interval $L\to\infty$. We obtain these solutions, solitons, numerically, and then analyze their stability. Our main objective is to construct the existence and stability chart on the (h,γ) plane. This chart will serve as the first step towards the complete attractor chart of Eq. (2), similarly to the attractor chart for the *parametrically* driven NLS

$$i\Psi_t+\Psi_{xx}+2|\Psi|^2\Psi=-i\gamma\Psi-he^{i\Omega t}\Psi^*, \tag{3}$$

which was constructed in Refs. [16,17].

Although the solitons [i.e., solutions with $\psi_x(\pm\infty)=0$] and soliton wave trains [for which $\psi(x+L)=\psi(x)$] may look qualitatively similar when plotted on a finite interval $(-L/2,L/2)$, their respective domains of existence are different. The stability of solutions is also very sensitive to the interval length; in particular, we demonstrate that, increasing L, the stability windows of Terrones *et al.*, ''close.'' There are no windows of stability on the stability chart of solitons $(L=\infty)$.

The paper is organized as follows. In Sec. II we consider the spatially homogeneous (flat) solution and analyze its stability. In Sec. III the upper and lower boundaries of existence domains of two solitons are found numerically. Section IV deals with the stability of the solitons. We show that one of the two solitons is always unstable and describe the stability region of the other one. The issue of stability windows is also addressed therein. Finally, in Sec. V our existence and stability chart is compared with results of direct numerical simulations available in the literature.

B. Relation to the sine-Gordon equation

Out of three parameters h,γ, and Ω, only two are significant. Indeed, if $\Psi(x,t)$ is a solution of Eq. (1) corresponding to h,γ, and Ω, $\tilde{\Psi}(x,t)=k\Psi(kx,k^2t)$ is the solution corresponding to $\tilde{h}=k^3h$, $\tilde{\Omega}=k^2\Omega$, and $\tilde{\gamma}=k^2\gamma$. Hence we may always fix, e.g., $\Omega=1$ and retain only h and γ as control parameters [14,15].

Next, the substitution $\Psi(x,t)=e^{it}\psi(x,t)$ reduces Eq. (1) to an autonomous equation

$$i\psi_t+\psi_{xx}-\psi+2|\psi|^2\psi=-i\gamma\psi-h. \tag{4}$$

In this paper we will always be using the representation (4). On several occasions we will touch upon the results of Terrones *et al.* [15]. These authors study the NLS equation, but present their conclusions for the externally driven sine-Gordon system, Eq. (1). The correspondence between Eqs. (1) and (4) is established by the formulas

$$q(\tau,z)=4\varepsilon\,\mathrm{Re}[i\psi(t,x)e^{-i\omega\tau}]+O(\varepsilon^3); \tag{5}$$

$$x=\varepsilon z,\quad t=\frac{\varepsilon^2}{2}\tau; \tag{6}$$

$$\alpha=\varepsilon^2\gamma,\quad \Gamma=4\varepsilon^3h, \tag{7}$$

where ε is the detuning of the sine-Gordon driving frequency from unity:

$$\omega=1-\frac{\varepsilon^2}{2}. \tag{8}$$

Equation (6) implies that the sine-Gordon interval length L_{SG} and the NLS interval L_{NLS} are related as

$$L_{\mathrm{NLS}}=\varepsilon L_{\mathrm{SG}}. \tag{9}$$

For example, the results of Ref. [15] obtained for $\omega=0.87,\alpha=0.04$, and $L_{\mathrm{SG}}=24$ correspond to our Eq. (4) with $\gamma=0.1538$ and $L_{\mathrm{NLS}}=12.24$.

II. FLAT-LOCKED SOLUTIONS: EXISTENCE AND STABILITY DOMAINS

A. Three branches of flat solutions

We start with the analysis of spatially homogeneous solutions $(\Psi_{xx}=0)$ locked to the driver's frequency: $\Psi(x,t)=\psi_0e^{it}$. The complex amplitude ψ_0 satisfies the algebraic equation

$$-\psi_0+2|\psi_0|^2\psi_0=-i\gamma\psi_0-h. \tag{10}$$

Equation (10) was, of course, discussed before [7]; for the most detailed analysis see [15]. We are, nevertheless, going to reconsider it here because we will need some facts about flat-locked solution in our study of solitons. The main distinction from the work of Terrones *et al.* is that we will consider Eq. (10) in the whole range of parameters, while those authors restricted themselves to *small* values of h and γ. Also note that there are some notational distinctions: (i) our NLS equation (2) has different coefficients with respect to those in [15]; (ii) our driver h is real and positive and ψ_0 is complex, whereas Terrones *et al.* work with complex h and real positive ψ_0; (iii) the conclusions of [15] are presented in the sine-Gordon rather than the NLS notation.

Writing $\psi_0=ae^{i\theta}$, Eq. (10) reduces to a system

$$-a+2a^3=-h\cos\theta, \tag{11}$$

$$\gamma a=h\sin\theta. \tag{12}$$

Eliminating θ, we obtain an equation cubic in $\rho_0=a^2$:

$$4\rho_0^3-4\rho_0^2+(1+\gamma^2)\rho_0-h^2=0. \tag{13}$$

Any positive root ρ_0 of this equation defines a flat-locked solution $\psi_0=\sqrt{\rho_0}e^{i\theta}$, where

$$\tan\theta=\frac{\gamma}{1-\rho_0}.$$

The analysis of Eq. (13) is straightforward. First of all, it cannot have real negative roots. (Substitute $\rho_0=-q$ and obtain a sum of four strictly negative terms.) Hence there are either three positive roots or one positive and two complex-conjugate roots. In terms of

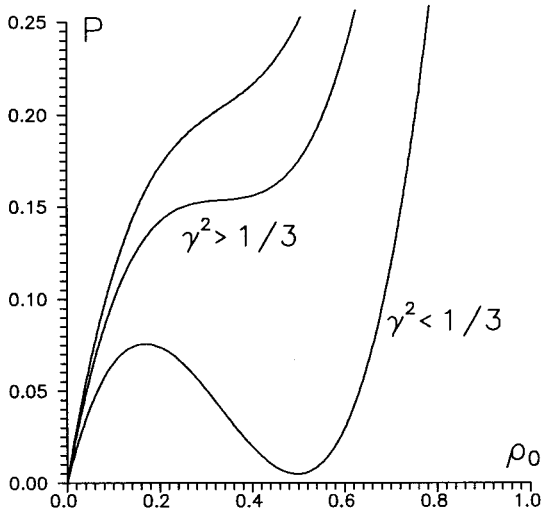

FIG. 1. Cubic $P(\rho_0)$ for $\gamma^2<1/3$ and $\gamma^2>1/3$. From left to right, $\gamma^2=0.5,\ 0.35$, and 0.01.

$$P(\rho_0)=\rho_0[4\rho_0^2-4\rho_0+(1+\gamma^2)],$$

Eq. (13) is rewritten as

$$P(\rho_0)=h^2. \tag{14}$$

When $\gamma^2\geqslant 1/3$, we have $dP/d\rho_0\geqslant 0$ and so Eq. (14) has just one real root, whereas when $\gamma^2<1/3$, there can be either one or three real roots (Fig. 1).

In the latter case the number of real roots is determined by the sign of the expression

$$Q=\left(\frac{\gamma^2-1/3}{3}\right)^3+\left(\frac{\gamma^2+1/9}{3}-h^2\right)^2.$$

If $Q<0$, there are three real roots; if $Q>0$, there is just one. After some algebra, this criterion translates to the following one:

$$\begin{aligned} &3 \text{ roots if } h_-(\gamma)\leqslant h\leqslant h_+(\gamma),\\ &1 \text{ root otherwise,}\end{aligned} \tag{15}$$

where

$$h_\pm(\gamma)\equiv\left\{\frac{1}{3}\left(\gamma^2+\frac{1}{9}\right)\pm\frac{1}{3}\sqrt{\frac{1}{3}\left(\frac{1}{3}-\gamma^2\right)^3}\right\}^{1/2}. \tag{16}$$

Summarizing, we have two cases. First, for $\gamma\geqslant 1/\sqrt{3}$ and all h, we have just one flat-locked solution (the right-hand curve in Fig. 2). Second, for $\gamma<1/\sqrt{3}$ (the left-hand curve in Fig. 2) we have three branches of solutions: there are three solutions for h lying between $h_-(\gamma)$ and $h_+(\gamma)$ and only one solution if h does not fall into this interval. The first (lowest) branch satisfies

$$0<|\psi_0|^2\leqslant\rho_-(\gamma);$$

the second (middle) branch is

$$\rho_-(\gamma)\leqslant|\psi_0|^2\leqslant\rho_+(\gamma);$$

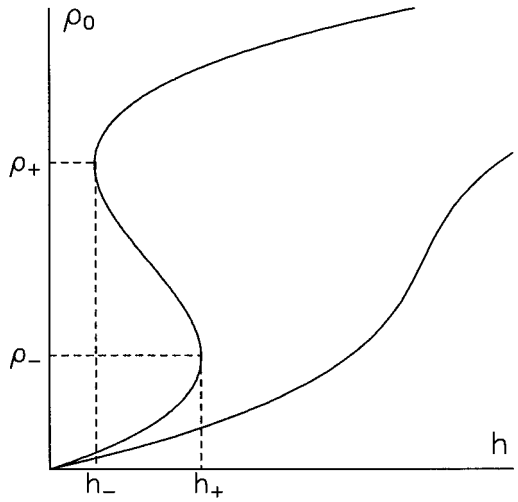

FIG. 2. Amplitude of the spatially homogeneous solution versus h. Left-hand curve, $\gamma<1/\sqrt{3}$; right-hand curve, $\gamma>1/\sqrt{3}$.

and the third, upper branch is given by

$$|\psi_0|^2\geqslant\rho_+(\gamma).$$

Here

$$\rho_\pm(\gamma)\equiv\frac{1}{3}\pm\frac{1}{6}\sqrt{1-3\gamma^2}. \tag{17}$$

B. Stability of flat solutions

Next we proceed to the stability of the flat-locked solutions. Taking $\psi(x,t)=\psi(x)+\delta\psi(x,t)$, where $\psi(x)$ is a stationary solution of Eq. (4) and $\delta\psi$ is a small perturbation, and linearizing Eq. (4) about $\psi(x)$ yields

$$J(y_t+\gamma y)=Hy.$$

Here $y(x,t)$ is a two-component column comprising of the real and imaginary parts of the perturbation

$$y(x,t)=\begin{pmatrix}\mathrm{Re}\,\delta\psi\\ \mathrm{Im}\,\delta\psi\end{pmatrix}$$

and H and J are 2×2 matrices

$$J=\begin{pmatrix}0 & -1\\ 1 & 0\end{pmatrix}, \tag{18}$$

$$H=\begin{pmatrix}-\partial^2+1-2(3\psi_R^2+\psi_I^2) & -4\psi_R\psi_I\\ -4\psi_R\psi_I & -\partial^2+1-2(3\psi_I^2+\psi_R^2)\end{pmatrix}, \tag{19}$$

where $\partial=\partial/\partial x$. Finally, $\psi_R(x)$ and $\psi_I(x)$ represent the real and imaginary parts of the solution $\psi(x)$ whose stability is examined. In the case at hand, ψ_R and ψ_I are the real and imaginary parts of the flat-locked solution ψ_0, i.e., $\psi_0=\psi_R+i\psi_I$.

Separating the time variable

$$y(x,t)=z(x)e^{\lambda t}, \tag{20}$$

we arrive at the eigenvalue problem

$$Hz(x)=\mu Jz(x), \tag{21}$$

where

$$\mu=\lambda+\gamma. \tag{22}$$

In general, μ and $z(x)$ are complex. The solution $\psi(x)$ will be stable if Eq. (21) does not have eigenvalues μ with the real part greater than γ.

In the case of the homogeneous solution $\psi(x)=\psi_0$, the eigenvalue μ and eigenvector $z(x)$ can be found explicitly. Writing $z(x)=z_0e^{-ikx}$, we obtain a matrix eigenvalue problem

$$(H_k-\mu J)z_0=0, \tag{23}$$

where

$$H_k=\begin{pmatrix} k^2+1-2(3\psi_R^2+\psi_I^2) & -4\psi_R\psi_I \\ -4\psi_R\psi_I & k^2+1-2(3\psi_I^2+\psi_R^2) \end{pmatrix},$$

with $\psi_R=\mathrm{Re}\psi_0$ and $\psi_I=\mathrm{Im}\psi_0$. Equating the determinant of $(H_k-\mu J)$ to zero, we finally arrive at

$$-\mu^2=(k^2+1-2|\psi_0|^2)(k^2+1-6|\psi_0|^2). \tag{24}$$

If $|\psi_0|^2\leqslant 1/6$, there are no k's such that

$$F(k^2)=(2|\psi_0|^2-1-k^2)(6|\psi_0|^2-1-k^2)$$

is negative and so $\mathrm{Re}\mu$ is always zero and the flat solution is stable. Let us now assume that $|\psi_0|^2>1/6$. Here we have to differentiate between two cases. First, if $|\psi_0|^2>1/4$, the minimum of the parabola $F(k^2)$ occurs at $k^2=4|\psi_0|^2-1>0$ and is equal to $F_{\min}=-4|\psi_0|^4$. The corresponding $\mathrm{Re}\mu$ is maximum and equals $2|\psi_0|^2$. Consequently, the peturbation $\delta\psi$ will grow in this case if $2|\psi_0|^2>\gamma$. (This is the case of the modulation instability.)

Second, if $1/6<|\psi_0|^2<1/4$, the minimum of $F(k^2)$ occurs at $k^2=0$. In this case $F_{\min}=(2|\psi_0|^2-1)(6|\psi_0|^2-1)$ and the perturbation will grow if

$$-(2|\psi_0|^2-1)(6|\psi_0|^2-1)>\gamma^2. \tag{25}$$

This is an instability with respect to spatially homogeneous perturbations. The inequality (25) amounts to

$$\rho_-(\gamma)<|\psi_0|^2<\rho_+(\gamma),$$

with $\rho_\pm$ as in Eq. (17). Notice that since $\rho_-(\gamma)<1/4$ only if $\gamma<1/2$, this type of instability may occur only in the region $\gamma<1/2$.

C. Summary of flat solutions

Summarizing, we have three typical situations.

(a) $0<\gamma<1/2$. This situation is presented in Fig. 3(a). We have three branches of flat solutions. The whole of the lowest branch is stable. [Here $|\psi_0|^2<\rho_-(\gamma)$ and $h<h_+(\gamma)$.] The whole of the upper branch as well as the upper part of the middle branch above $|\psi_0|^2=1/4$ are modulationally unstable. Finally, the lower part of the middle branch $\rho_-(\gamma)<|\psi_0|^2<1/4$ is unstable with respect to flat perturbations.

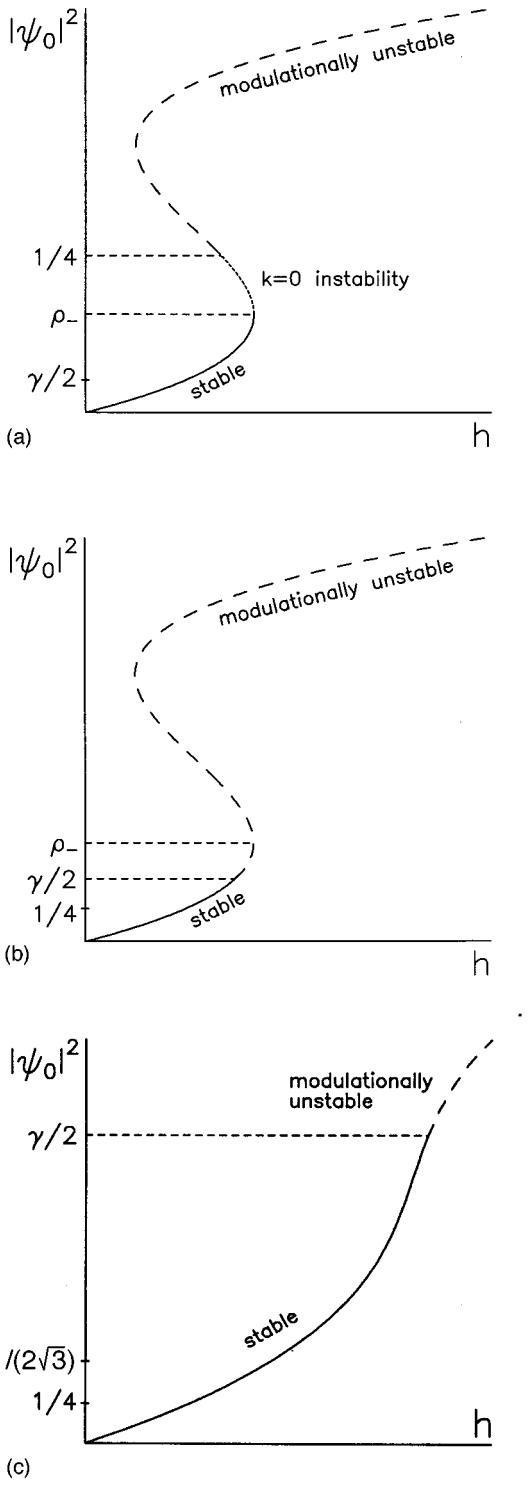

FIG. 3. Flat-locked solutions and their stability. (a) $\gamma<1/2$, (b) $1/2<\gamma<1/\sqrt{3}$, and (c) $\gamma>1/\sqrt{3}$. Solid line, stable; long-dashed line, unstable against spatially inhomogeneous perturbations; short-dashed line, unstable against spatially homogeneous perturbations.

(b) $1/2<\gamma<1/\sqrt{3}$. This situation is shown in Fig. 3(b). Similarly to the case $\gamma<1/2$, we have three branches here. However, only a part of the lower branch, namely, $|\psi_0|^2<\gamma/2$, is stable. The rest of it as well as the other two

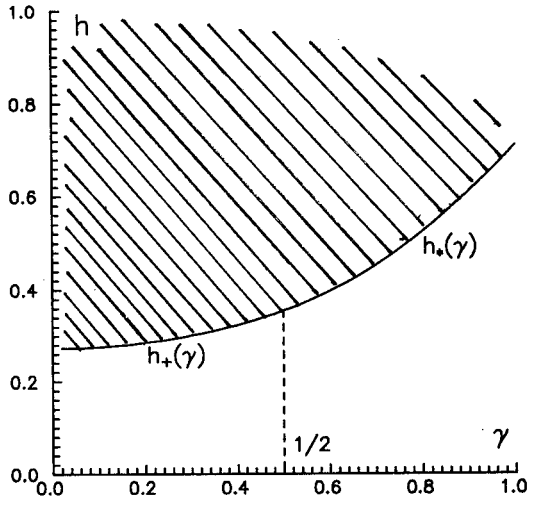

FIG. 4. Regions of stability (blank) and instability (shaded) of the flat-locked solution on the (h,γ) plane.

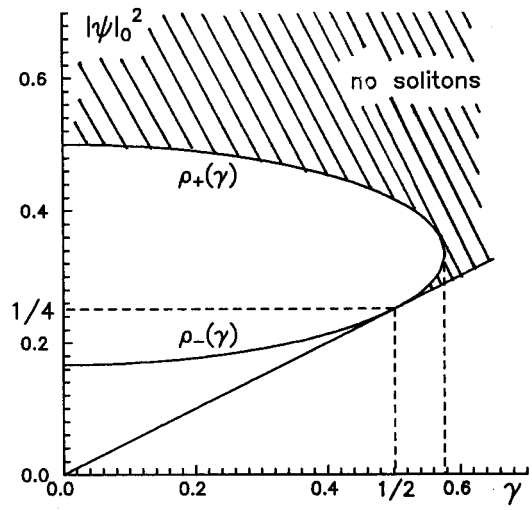

FIG. 5. Asymptotic value $|\psi_0|^2$ versus the damping coefficient γ. The shaded region is where no solitons can exist due to the asymptotic exclusion principle.

branches, are modulationally unstable. In terms of h and γ, the inequality $|\psi_0|^2<\gamma/2$ translates into $h<h_*(\gamma)$, where

$$h_*(\gamma)\equiv\sqrt{\gamma^3-\gamma^2+\gamma/2}. \tag{26}$$

(c) $\gamma>1/\sqrt{3}$. This situation is depicted in Fig. 3(c). There is just one branch that is stable for $|\psi_0|^2<\gamma/2$ [i.e., for $h<h_*(\gamma)$] and modulationally unstable otherwise.

Finally, our (h,γ) plane is decomposed into two infinite regions; see Fig. 4. A stable homogeneous solution exists in the blank region; the domain of instability has been shaded. The boundary between the two regions is given by

$$h(\gamma)=\begin{cases} h_+(\gamma), & \gamma\leqslant 1/2 \\ h_*(\gamma), & \gamma\geqslant 1/2. \end{cases} \tag{27}$$

III. SOLITONS

A. Asymptotic behavior

Another type of insight provided by the analysis of the flat solutions is into the asymptotic behavior of *spatially localized* solutions. Indeed, if $\psi(x)$ is a static solution approaching asymptotically the value ψ_0, then denoting $\delta\psi=\psi(x)-\psi_0$ we find that

$$y(x)=\begin{pmatrix} \mathrm{Re}\,\delta\psi \\ \mathrm{Im}\,\delta\psi \end{pmatrix}$$

satisfies

$$Hy(x)=\gamma Jy(x), \tag{28}$$

with J and H as in (18) and (19). Writing $y(x)=e^{-ikx}$, we obtain

$$(k^2+1-2|\psi_0|^2)(k^2+1-6|\psi_0|^2)=-\gamma^2. \tag{29}$$

This equation has two roots k_1^2 and k_2^2. Consequently, the general solution of Eq. (28) is a sum of four exponentials $e^{\pm ik_1x}$ and $e^{\pm ik_2x}$. If both k_1 and k_2 are real for certain $|\psi_0|$, $y(x)$ is not localized and so Eq. (4) cannot have localized solution in the corresponding region. Both k_1^2 and k_2^2 are positive if the following three conditions are satisfied simultaneously: (i) The discriminant of (29) is positive

$$|\psi_0|^2>\frac{\gamma}{2}, \tag{30}$$

(ii) the product of two roots is positive

$$(2|\psi_0|^2-1)(6|\psi_0|^2-1)+\gamma^2>0, \tag{31}$$

and (iii) the sum of two roots is positive

$$8|\psi_0|^2-2>0. \tag{32}$$

Again, we have to consider several cases.

If $\gamma>1/\sqrt{3}$, the condition (30) is stronger than (32), while (31) is satisfied for all $|\psi_0|$. This means that the condition for the solitons nonexistence is simply $|\psi_0|^2>\gamma/2$ or, in terms of h and γ, $h>h_*(\gamma)$, where h_* is as in Eq. (26).

If $1/2<\gamma<1/\sqrt{3}$, the inequality (30) is still stronger than (32), while Eq. (31) amounts to

$$|\psi_0|^2\in(0,\rho_-)\cup(\rho_+,\infty). \tag{33}$$

Taking the intersection of (33) and (30), one gets

$$|\psi_0|^2\in\left(\frac{\gamma}{2},\rho_-\right)\cup(\rho_+,\infty),$$

where $\rho_\pm=\rho_\pm(\gamma)$ are as in Eq. (17).

Finally, when $\gamma<1/2$, Eq. (32) is stronger than (30), while ρ_- is smaller than 1/4. Thus the intersection of (33) and (32) is simply

$$|\psi_0|^2>\rho_+(\gamma).$$

These conclusions are summarized in Figs. 5 and 6. In Fig. 5, dashed is the region where the solitons' existence is excluded by the above asymptotic reasoning. In principle, solitons could have existed for ψ_0 on the middle branch [i.e.,

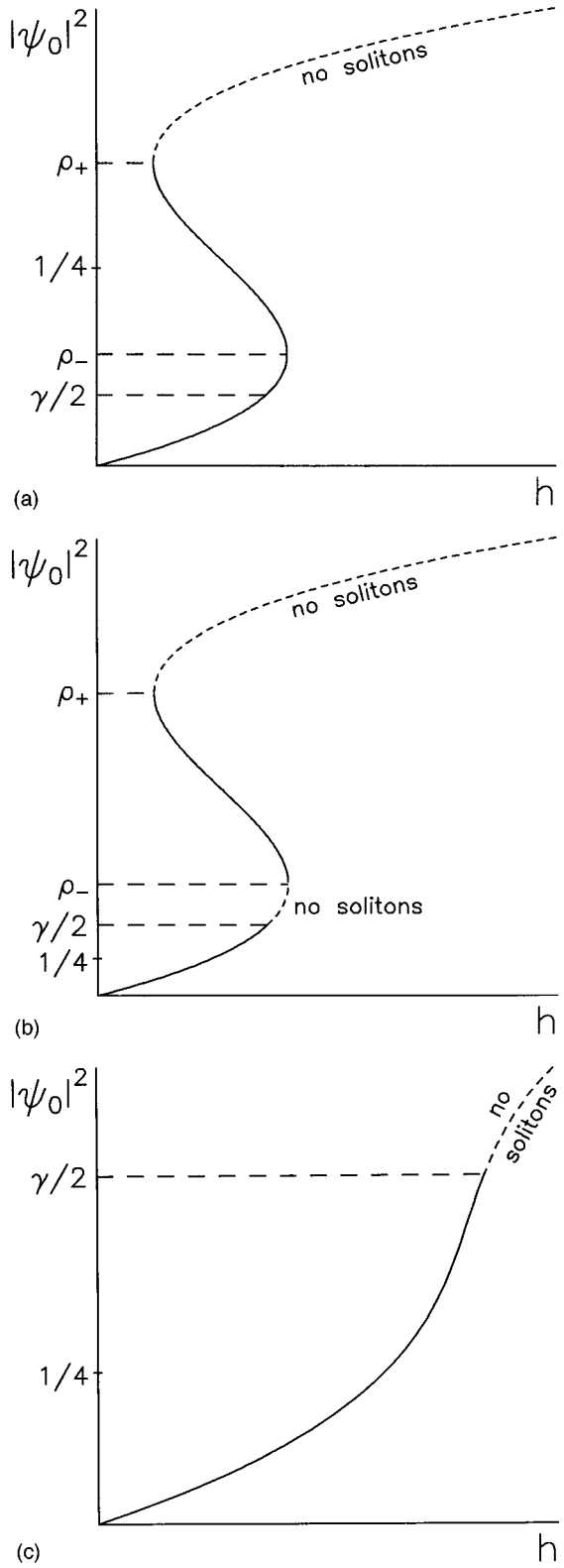

FIG. 6. Asymptotic value of the soliton $|\psi_0|^2$ versus the driver's strength h. Dashed lines, no solitons are possible with such a $|\psi_0|^2$; solid lines, solitons with these asymptotic values are not excluded by the asymptotic reasoning. (a) $\gamma<1/2$, (b) $1/2<\gamma<1/\sqrt{3}$, and (c) $\gamma>1/\sqrt{3}$.

between the curves $|\psi_0|^2=\rho_-(\gamma)$ and $|\psi_0|^2=\rho_+(\gamma)$ in Fig. 5]. In this case one pair of exponents $k_{1,2}$ is imaginary and the other one ($k_{3,4}$) is real. However, no solitons with asymptotic values on the middle branch were found (see Sec. III D). As we will show below, solitons exist only below the line

$$|\psi_0|^2=\begin{cases}\rho_-(\gamma), & \gamma\leqslant 1/2\\ \gamma/2, & \gamma\geqslant 1/2.\end{cases}$$

Consequently, the soliton's existence region lies on the lowest branch of $|\psi_0|$ [see Figs. 6(a)–6(c)].

Our final remark in this subsection is on the way the soliton approaches its asymptotic value. Here our interest is motivated by indications that solitons with undulations on their spatial ''tails'' can form bound states [18]. For $|\psi_0|^2<\gamma/2$, the exponents k_1 and k_2 are a pair of complex-conjugate values with nonzero real part. Consequently, each of the four exponentials undergoes undulations. On the other hand, when $\gamma<1/2$ there is a region on the $(|\psi_0|^2,\gamma)$ plane where both k_1^2 and k_2^2 are negative. This region is defined by the intersection of Eq. (31) and the inequality $|\psi_0|^2<1/4$; it is not difficult to realize that the intersection is

$$\frac{\gamma}{2}<|\psi_0|^2<\rho_-(\gamma). \tag{34}$$

In this region solitons approach their asymptotic values monotonically; according to [18], no bound states of solitons may emerge under such circumstances. This region pertains to the lowest branch of the flat-locked solutions. In terms of h and γ, Eq. (34) can be rewritten as

$$h_*(\gamma)<h<h_+(\gamma) \quad \left(\gamma\leqslant\frac{1}{2}\right). \tag{35}$$

B. Numerical solutions: Method

For $\gamma=0$, the equation

$$\psi_{xx}-\psi+2|\psi|^2\psi=-i\gamma\psi-h \tag{36}$$

admits a pair of exact soliton solutions [14]

$$\psi_\pm(x)=\psi_0\left(1+\frac{2\sinh^2\alpha}{1\pm\cosh\alpha\,\cosh(Ax)}\right). \tag{37}$$

Here α is defined by

$$h=\frac{\sqrt{2}\cosh^2\alpha}{(1+2\cosh^2\alpha)^{3/2}}; \tag{38}$$

$h(\alpha)$ being a monotonically decreasing function, α is uniquely determined by h. Next, ψ_0 is the asymptotic value of both ψ_- and ψ_+ solitons:

$$\psi_\pm(x)\to\psi_0 \quad \text{as} \quad |x|\to\infty;$$

ψ_0 is real and positive:

$$\psi_0=\frac{1}{\sqrt{2(1+2\cosh^2\alpha)}}. \tag{39}$$

Finally, A has the meaning of ''half the area'' of ψ_+ and ψ_- and is equal to

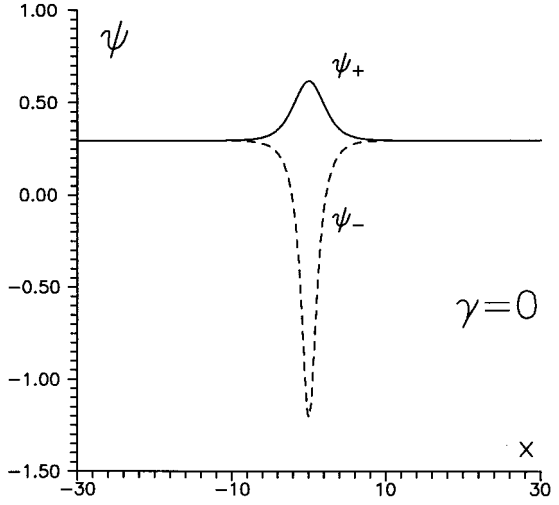

FIG. 7. ψ_+ and ψ_- solitons in the undamped case $\gamma=0$. These solutions are given by explicit formulas, Eqs. (37). The behavior of $\psi_\pm(x)$ is qualitatively similar for all h; in this plot $\alpha=1$ ($h=0.243$).

$$A=2\psi_0\ \sinh\ \alpha=\frac{1}{2}\int(\psi_\pm^2-\psi_0^2)dx=\frac{\sinh\alpha}{\sqrt{1+2\cosh^2\alpha}}. \tag{40}$$

Solutions $\psi_+(x)$ and $\psi_-(x)$ are plotted in Fig. 7. The domain of existence of both of these extends from $\alpha=0$ to $\alpha=\infty$ or, in terms of the driver's strength, from $h=0$ to $h=\sqrt{2/27}\approx 0.2722$.

For $\gamma>0$, no exact solutions are available. We therefore had to obtain solitons numerically. Our numerical scheme was based on the continuous analog of Newton's method (see [19] for review and references).

The finite difference version of Eq. (36), together with the discretized version of the open-end boundary conditions $\psi_x(\pm L/2)=0$, can be written in the form

$$\mathbf{G}(\boldsymbol{\psi})=0, \tag{41}$$

where $\boldsymbol{\psi}=(\psi_0,\psi_1,\ldots,\psi_{N+1})$ is the discretized solution, with $\psi_n=\psi(x_n)$, $x_n=-L/2+n\Delta x$, $\Delta x=L/(N+1)$, and $\mathbf{G}=(G_0,G_1,\ldots,G_{N+1})$ is a nonlinear operator defined by

$$G_n=\frac{\psi_{n+1}+\psi_{n-1}-2\psi_n}{(\Delta x)^2}-\psi_n+2|\psi_n|^2\psi_n+i\gamma\psi_n+h,$$

for $n=1,2,...,N$, and

$$G_0=\frac{-3\psi_0+4\psi_1-\psi_2}{2\Delta x},$$

$$G_{N+1}=\frac{\psi_{N-1}-4\psi_N+3\psi_{N+1}}{2\Delta x}.$$

(Notice that we use a second-order finite difference approximation both for ψ_{xx} and ψ_x.)

The idea of the continuous analog of Newton's method is to introduce an auxiliary ''evolution'' parameter τ in such a way that $\boldsymbol{\psi}$ satisfies the differential equation

$$\frac{d}{d\tau}\mathbf{G}(\boldsymbol{\psi}(\tau))+\mathbf{G}(\boldsymbol{\psi}(\tau))=\mathbf{0}, \tag{42}$$

with the initial condition

$$\boldsymbol{\psi}(0)=\boldsymbol{\psi}^{(0)}. \tag{43}$$

Here $\boldsymbol{\psi}^{(0)}$ is an initial guess for the soliton solution. Since $\mathbf{G}(\boldsymbol{\psi}(\tau))\to\mathbf{0}$ as $\tau\to\infty$, $\boldsymbol{\psi}(\infty)$ satisfies Eq. (41). Our iteration algorithm is based on the discretization of Eq. (42) with respect to τ:

$$\boldsymbol{\psi}^{(\alpha+1)}=\boldsymbol{\psi}^{(\alpha)}-\Delta\tau^{(\alpha+1)}\left(\frac{\partial\mathbf{G}}{\partial\boldsymbol{\psi}}\right)^{-1}_{\boldsymbol{\psi}=\boldsymbol{\psi}^{(\alpha)}}\mathbf{G}(\boldsymbol{\psi}^{(\alpha)}), \tag{44}$$

where $\alpha=0,1,2,\ldots$ and $\Delta\tau^{(\alpha+1)}=\tau^{(\alpha+1)}-\tau^{(\alpha)}$ is chosen so as to minimize the residual

$$\delta^{(\alpha)}=\max_{1\le n\le N}\{|\mathrm{Re}G_n(\boldsymbol{\psi}^{(\alpha)})|,|\mathrm{Im}G_n(\boldsymbol{\psi}^{(\alpha)})|\}. \tag{45}$$

(For details see [19].)

Our continuation strategy was as follows. First, we used the exact solutions (37) as an initial approximation for $\gamma=0.02$ and h in the middle of the interval $(0,\sqrt{2/27})$, i.e., for $h=0.136$. Second, we utilized the obtained numerical solutions as initial approximations for the same $\gamma=0.02$ and h above and below 0.136. We advanced along the h axis until the Newtonian iterations ceased to converge. The absence of convergence may be caused by a bad initial approximation; for this reason we had to decrease the increment Δh in the neighborhood of the boundaries of the domain of existence. As a result, we were able to establish both the upper and the lower boundaries with the desired accuracy; see below. Next, taking the numerical solutions at approximately the middle of the domain of existence for $\gamma=0.02$, we employed them as initial approximations for the same h with $\gamma=0.04$, then advanced up and down in h, and the process repeated.

The bulk of calculations was performed on an interval $(-L/2,L/2)=(-30,30)$, with the exception of the neighborhood of the upper boundary of the domain of existence, where the solitons decay very slowly in x. In this neighborhood the interval length L was increased appropriately. Generically, we utilized the second-order Newtonian algorithm with the grid spacing $\Delta x=0.1$; the neighborhood of the upper boundary was again an exception (see Sec. III D).

Similarly to the case when $\gamma=0$, in the case of nonzero dissipation solitons generically come in pairs. By analogy with the $\gamma=0$ case, we denote them $\psi_+(x)$ and $\psi_-(x)$. Figure 8 shows their profiles for several typical h. Here we have chosen values of h not very close to the lower boundary; the behavior of solutions in the neighborhood of the lower boundary can be quite peculiar (see Fig. 10 below).

C. Existence domain: Lower boundary

The value of h demarcating the lower boundary is usually referred to as the *threshold* driving strength: for a given γ, no localized solutions are possible for $h<h_{\mathrm{thr}}$. Kaup and

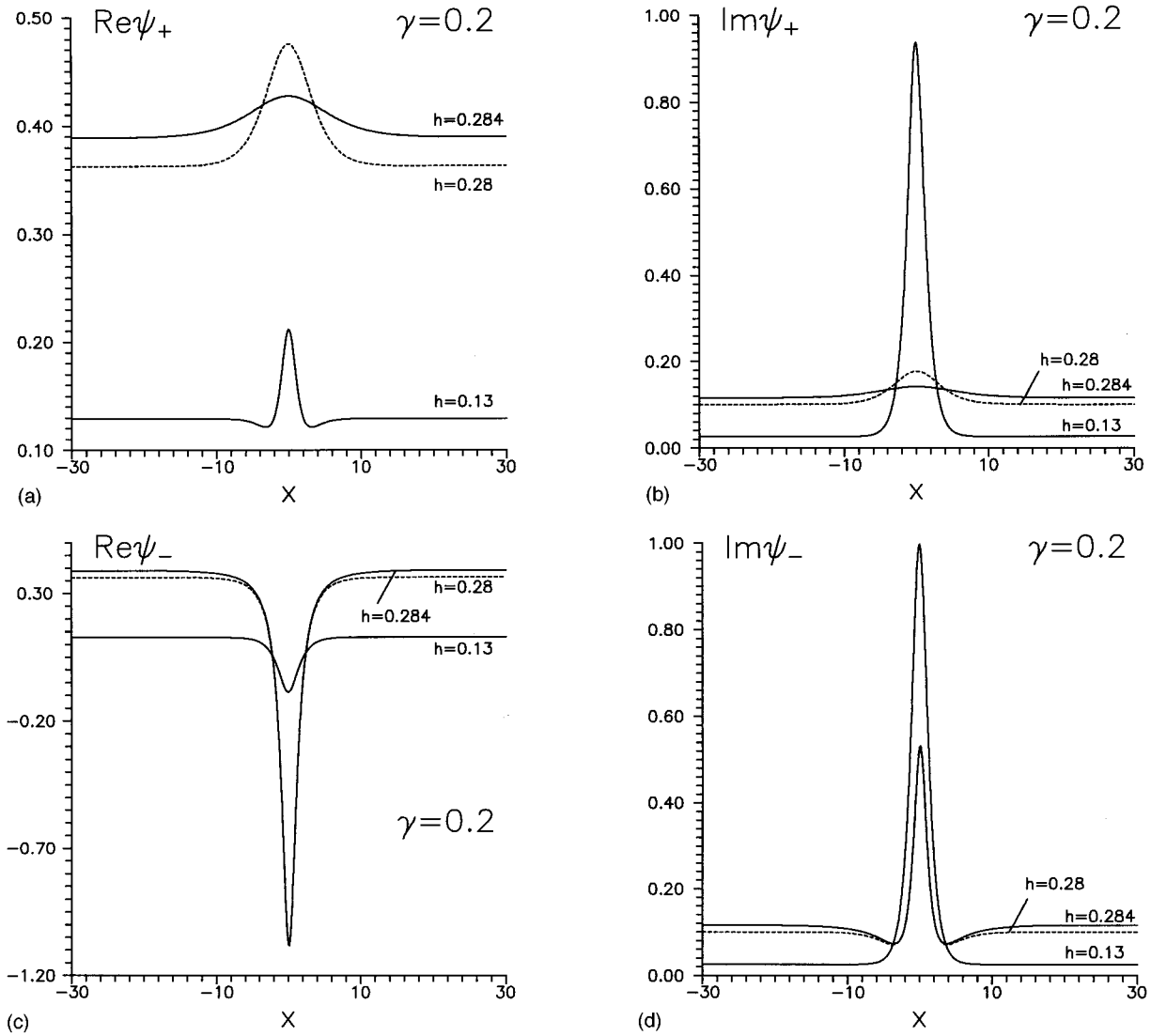

FIG. 8. Real and imaginary parts of the ψ_+ and ψ_- solitons in the region $\gamma<1/2$. Here $\gamma=0.2$; the value $h=0.130$ is close to the lower boundary of the existence domain ($h_{\rm thr}=0.127$), but not exceedingly so. The points $h=0.28$ and 0.284 represent solutions in the neighborhood of the upper boundary ($h_+=0.2845$).

Newell have found [1], by means of the inverse scattering-based perturbation theory, the following estimate for the threshold value:

$$h_{\rm thr}=\frac{2}{\pi}\gamma. \tag{46}$$

Spatschek *et al.* [11] and Terrones *et al.* [15] reproduced Eq. (46) by expanding $\psi_-(x)$ in a perturbation series in powers of small h and γ.

The threshold value that we have found numerically is plotted in Fig. 13 at the end of this section. For comparison, we have also plotted the straight line $h=(2/\pi)\gamma$ in the same picture. Surprisingly, the deviation of the actual $h_{\rm thr}$ from $(2/\pi)\gamma$ is extremely small even for not very small γ. For example, for $\gamma=0.48$ we have

$$\frac{h_{\rm thr}}{\gamma}-\frac{2}{\pi}=10^{-3}; \tag{47}$$

for $\gamma<0.48$ the above difference is even smaller. However, as γ grows beyond $\gamma\approx 0.5$, the actual $h_{\rm thr}$ gradually deviates from $(2/\pi)\gamma$.

For $h=h_{\rm thr}$ the two branches of localized solutions $\psi_+(x)$ and $\psi_-(x)$ merge. The point $h=h_{\rm thr}$ is a turning point therefore. We illustrate this fact by plotting $|\psi(0)|^2$, the modulus squared of the value of $\psi_\pm(x)$ in the middle of the interval, as a function of h (Fig. 9).

It is interesting to follow the evolution of ψ_+ and ψ_- when h approaches the threshold value from above. The transformation of ψ_+ into ψ_- is illustrated in Fig. 10.

D. Existence domain: Upper boundary

Let us now turn to the *upper* boundary of the existence domain. The upper boundary is different for ψ_+ and ψ_- solitons and depends on γ. Three typical regions can be identified as follows.

(a) $0\leqslant\gamma\leqslant 1/2$. Here we have three branches of flat solutions ψ_0 [Fig. 3(a)]; the lowest branch is stable and the other

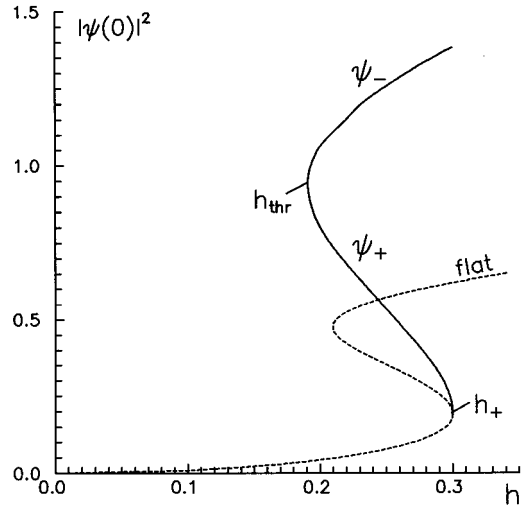

FIG. 9. Modulus squared of the $\psi_{\pm}$ solitons in the middle of the interval $x=0$ (solid line). Lower branch, $|\psi_{+}(0)|^2$; upper branch, $|\psi_{-}(0)|^2$; the two branches merge at the turning point $h_{\rm thr}=0.191\,03$. Also shown is the flat solution $|\psi_0|^2$ (dashed line). The branch $|\psi_{+}(0)|^2$ merges with $|\psi_0|^2$ at $h_{+}=0.300\,23$. In this plot $\gamma=0.3$.

two branches are unstable. All numerically found solitons ψ_{+} and ψ_{-} have their asymptotic values lying on the lowest branch. It is natural to assume that the upper boundary of the domain of existence of the ψ_{+} and ψ_{-} coincides with the point $h=h_{+}(\gamma)$, $|\psi_0|^2=\rho_{-}(\gamma)$, which separates the lowest branch of $|\psi_0|^2$ from the adjacent branch. We have verified this hypothesis numerically.

Our strategy was to find the solitons ψ_{+} and ψ_{-} with the asymptotic value $|\psi_0|^2$ as close to ρ_{-} as possible. As a closest asymptotic value we adopted $\tilde{\rho}(\gamma)=\rho_{-}(\gamma)-1.0\times10^{-3}$ and examined an equidistant set of γ's between 0 and 1/2 ($\gamma=0.02,0.04,0.06,\ldots,0.48$). For all these γ we were able to find both ψ_{+} and ψ_{-} solitons with the asymptotic value $|\psi_0|^2=\tilde{\rho}(\gamma)$. Consequently, we can assert that the upper boundary of the existence domain (expressed in terms of $|\psi_0|^2$) is not farther away than 10^{-3} from the value $|\psi_0|^2=\rho_{-}(\gamma)$. In terms of h, the proximity is even closer. Deviating $|\psi_0|^2$ from ρ_{-} by $\Delta(|\psi_0|^2)=10^{-3}$ results in the deviation Δh in h; this deviation can be easily found by means of the explicit formula Eq. (13):

$$h=\sqrt{4|\psi_0|^6-4|\psi_0|^4+(1+\gamma^2)|\psi_0|^2}. \tag{48}$$

For $\gamma<1/2$ the above deviation is $\sim10^{-6}$. (More precisely, as γ is increased from $\gamma=0.02$ through $\gamma=0.48$, the deviation Δh decreases from $\Delta h=3.7\times10^{-6}$ through $\Delta h=1.6\times10^{-6}$.) The smallness of Δh is explained, of course, by the fact that the derivative $dh/d|\psi_0|^2$ goes to zero as $|\psi_0|^2\to\rho_{-}$.

Parameters of our numerical scheme were chosen consistently with the smallness of the increments Δh. In order to be able to approach the value $h=h_{+}$ as close as the distance $\Delta h\sim10^{-6}$, we had to require the residual (45) to be not larger than $\delta^{(\alpha)}=10^{-7}$. Here we took the second-order Newtonian algorithm with $\Delta x=10^{-3}$, i.e., the truncation error was of order $(\Delta x)^2=10^{-6}$.

Since we were looking for *even* solutions, it was sufficient to solve Eq. (36) on a half interval $(0,L/2)$ with the boundary conditions $\psi_x(0)=\psi_x(L/2)=0$. When $x\to\infty$, the solitons decay to the value ψ_0 exponentially, as $\exp(-|{\rm Im}k|x)$, where k is given by Eq. (29). When γ grows from 0.02 to 0.48, the exponent $|{\rm Im}k|$ corresponding to $|\psi_0|^2=\tilde{\rho}$ grows from 0.07 to 0.2. Consequently, choosing the half-interval length $L/2=300$ we ensured that $|\psi_{\pm}(L/2)-\psi_0|$ would not exceed 10^{-9}.

Thus our numerical study shows that in the region $0<\gamma<1/2$ the upper boundary of the existence domain (for both ψ_{+} and ψ_{-} solitons) is given by $|\psi_0|^2=\rho_{-}(\gamma)$ or, in terms of the driver's strength, by $h=h_{+}(\gamma)$. As we approach the knee of the hysteresis curve $|\psi_0|^2=|\psi_0|^2(h)$, i.e., as $|\psi_0|^2\to\rho_{-}$, the soliton $\psi_{+}(x)$ flattens out so that when $h=h_{+}(\gamma)$, the $\psi_{+}(x)$ merges with the flat solution: $\psi_{+}(x)=\psi_0$. [See Figs. 8(a) and 8(b).] This is in agreement with the asymptotic analysis presented in Sec. III C, where we have shown that as $h\to h_{+}(\gamma)$ and $|\psi_0|\to\rho_{-}(\gamma)$, the decay exponents $k_{1,2,3,4}\to0$.

The second solution $\psi_{-}(x)$ does not flatten out as we approach the hysteresis knee, although the decay exponents do go to zero. The solution ψ_{-} remains localized [Figs. 8(c) and 8(d)], but the decay becomes *polynomial* not exponential. In the undamped case $\gamma=0$, this can be demonstrated explicitly. Sending $\alpha\to0$ ($h\to\sqrt{2/27}$) in Eq. (37) yields

$$\psi_{-}(x)\to\frac{1}{\sqrt{6}}\,\frac{x^2-27/2}{x^2+9/2}.$$

(b) $1/2<\gamma<1/\sqrt{3}\approx0.5774$. In this region the curve $|\psi_0|^2=|\psi_0|^2(h)$ is similar to case (a); there are three branches. However, the flat solution loses its stability not at the knee point but earlier, at $|\psi_0|^2=\gamma/2$ [Fig. 3(b)]. On the other hand, we know from the discussion in Sec. III A that there can be no solitons with $|\psi_0|^2$ on the lowest branch above $|\psi_0|^2=\gamma/2$. Consequently, it is natural to assume that the upper boundary of the soliton's existence domain, for both ψ_{+} and ψ_{-}, corresponds to $|\psi_0|^2=\gamma/2$. We examined this hypothesis using the same criterion as in the region $\gamma<1/2$. Surprisingly, the results for ψ_{+} and ψ_{-} turned out to be different.

We examined $\gamma=0.52$, 0.54, and 0.56. For all these γ's we were able to find the ψ_{+} soliton at the distance $\Delta(|\psi_0|^2)=1.0\times10^{-3}$ away from the value $|\psi_0|^2=\gamma/2$, i.e., for $|\psi_0|^2=(\gamma/2)-1.0\times10^{-3}$. The ψ_{+} solution is shown in Fig. 11.

As far as ψ_{-} is concerned, the upper boundary of its domain of existence was seen to deviate substantially from $\gamma/2$. Namely, for $\gamma=0.52$ we were unable to find the ψ_{-} soliton for $|\psi_0|^2$ closer than 6×10^{-3} to $\gamma/2$; for $\gamma=0.54$ and 0.56 this gap was 8×10^{-3} and 11×10^{-3}, respectively. (See Table I.) Here the parameters of the numerical scheme were $\Delta x=10^{-3}$, $\delta^{(\alpha)}=10^{-7}$, and $L/2=600$. We do not plot the ψ_{-} solitons as they look qualitatively similar to those arising in the region $\gamma<1/2$.

(c) $\gamma>1/\sqrt{3}$. In this region there is only one branch of flat solutions for each h. Similarly to case (b), the flat solution becomes unstable for $|\psi_0|^2>\gamma/2$ and similarly to that case, there can be no solitons in the region $|\psi_0|^2>\gamma/2$. Our nu-

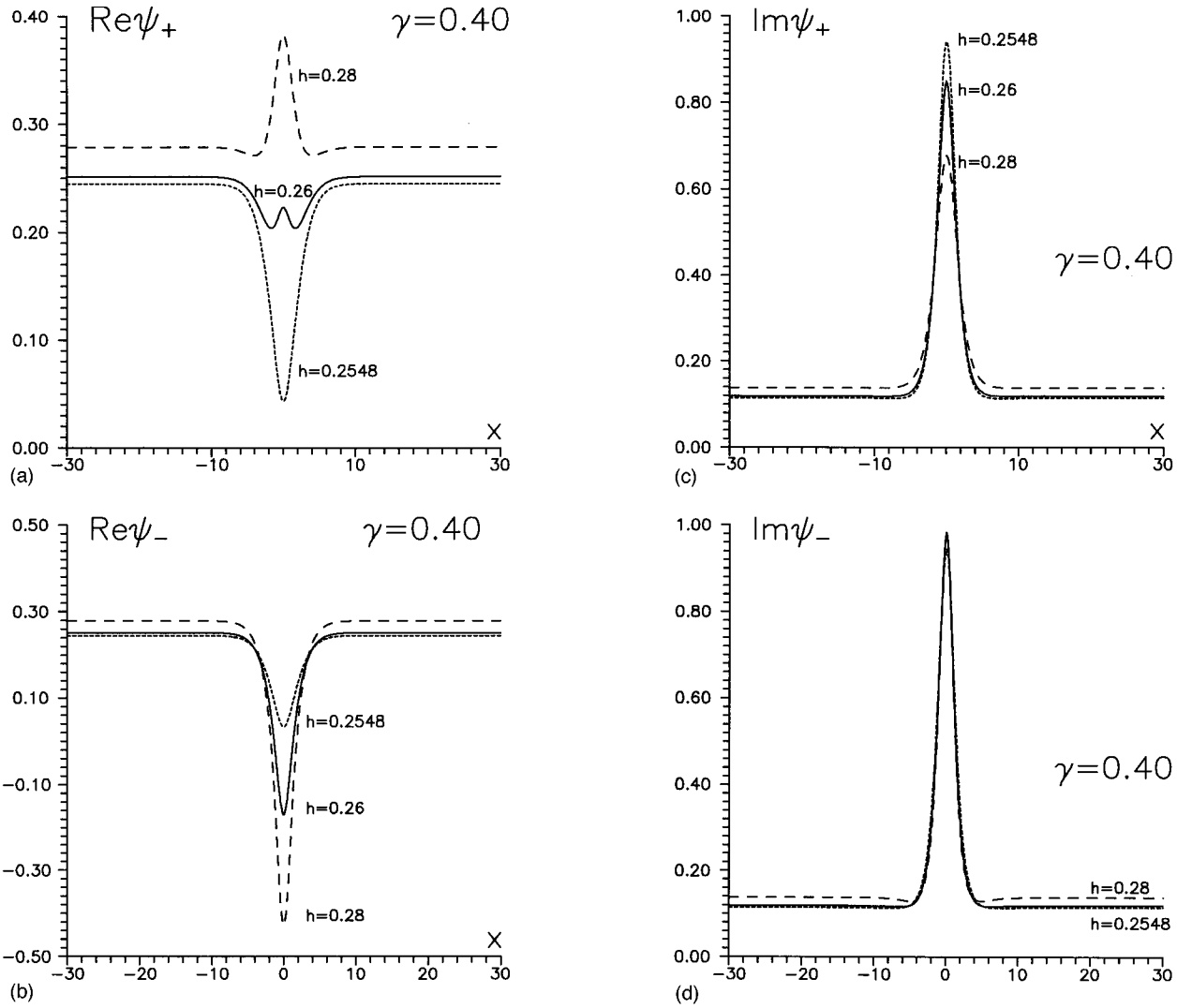

FIG. 10. Transformation of the $\psi_{\pm}$ solitons as h approaches h_{thr}, the lower boundary of their domain of existence. Long-dashed line, $h=0.28$; solid line, $h=0.26$; short-dashed line, $h=h_{\mathrm{thr}}=0.2548$. For $h=0.2548$, ψ_+ and ψ_- become indistinguishable. Notice a change of scale in (b) compared to (a).

merical results in this region are also similar to case (b). The ψ_+ soliton exists for values of $|\psi_0|^2$ up to and including $(\gamma/2)-10^{-3}$. On the other hand, the upper boundary of the existence domain for the ψ_- soliton was seen to be lower than $(\gamma/2)-10^{-3}$ (see Table I). Figure 12 gives the profiles of the ψ_+ and ψ_- solitons in the region $\gamma>1/\sqrt{3}$. The numerical parameters in the vicinity of the upper boundary were $\Delta x=10^{-3}$, $\delta^{(\alpha)}=10^{-7}$, and $L/2=600$.

E. Soliton existence region: Summary

Our conclusions are summarized in Fig. 13. The upper dashed line is given by Eq. (27) and demarcates the upper boundary of the domain of existence of the ψ_+ soliton. The upper solid line shows the upper boundary for the ψ_- soliton's domain of existence. For $\gamma<1/2$ this boundary is given by the same equation (27), whereas for $\gamma>1/2$ it deviates from Eq. (27). This deviation is, however, quite small ($\Delta h\sim 10^{-5}-10^{-4}$) and not visible in the plot.

The lower dashed line is a straight line $h=(2/\pi)\gamma$; it yields an approximation for the lower boundary of the domain of existence. The actual lower boundary h_{thr} (which is the same for both ψ_+ and ψ_- solitons) is shown by the lower solid line. Again, the dashed and solid lines are graphically indistinguishable.

Finally, the middle solid line is the stability boundary of the ψ_- soliton. It will be discussed below (Sec. IV B).

IV. STABILITY OF SOLITONS

A. Spectrum structure

To analyze the stability of the ψ_+ and ψ_- solitons, we numerically solved the eigenvalue problem (21) with H as in Eq. (19), with $\psi_R(x),\psi_I(x)$ being the real and imaginary parts of the corresponding soliton solution (found numerically beforehand). The solution is considered stable if $\mathrm{Re}\mu<\gamma$ for all eigenvalues μ.

Continuous spectrum. Before proceeding to results of the computation, we need to describe the spectrum structure of the operator $J^{-1}H$. When $|x|\to\infty$, the solitons $\psi_{\pm}(x)$ approach the value ψ_0, Eq. (21) reduces to a matrix eigenvalue problem (23), and the eigenvalue μ and wave number k are

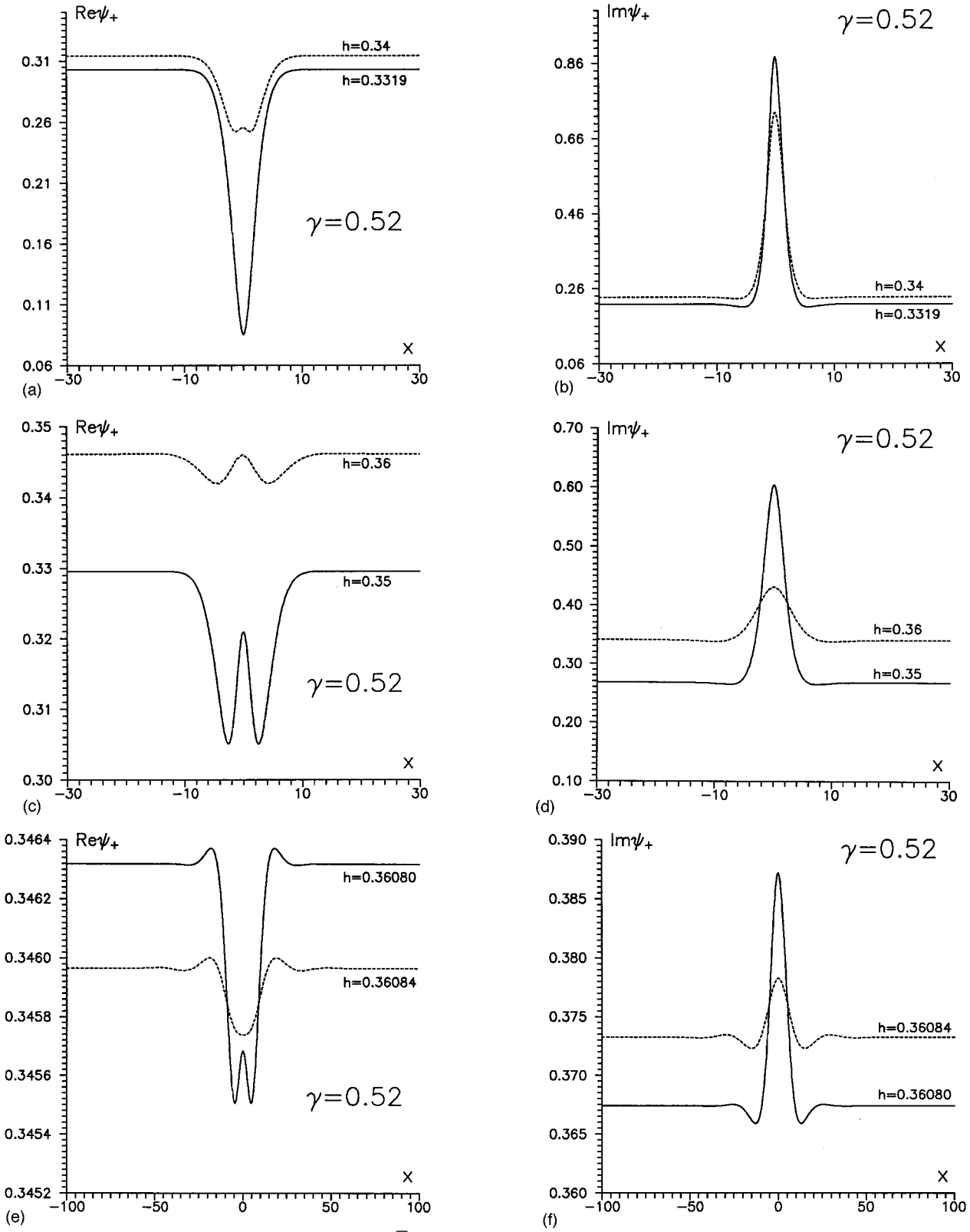

FIG. 11. ψ_+ soliton in the second region ($1/2<\gamma<1/\sqrt{3}$). In this plot $\gamma=0.52$. The transformation of ψ_+ is shown as h is increased from $h_{\rm thr}=0.3319$ through $h=0.360\,840$, which is close to the upper boundary of the existence domain $h_*=0.360\,843$.

related by the dispersion formula (24). The number of real roots $k_1,k_2,\ldots$ of Eq. (24) determines the multiplicity of the continuous spectrum.

When $|\psi_0|^2<1/6$, the continuous spectrum occupies the whole imaginary axis of μ outside the gap $-\omega_0<\mathrm{Im}\mu<\omega_0$, where

$$\omega_0=\sqrt{(2|\psi_0|^2-1)(6|\psi_0|^2-1)}. \tag{49}$$

When $|\psi_0|^2>1/6$, the continuous spectrum fills in the entire imaginary axis and the region $-\nu\leqslant\mathrm{Re}\mu\leqslant\nu$ on the real axis. Here

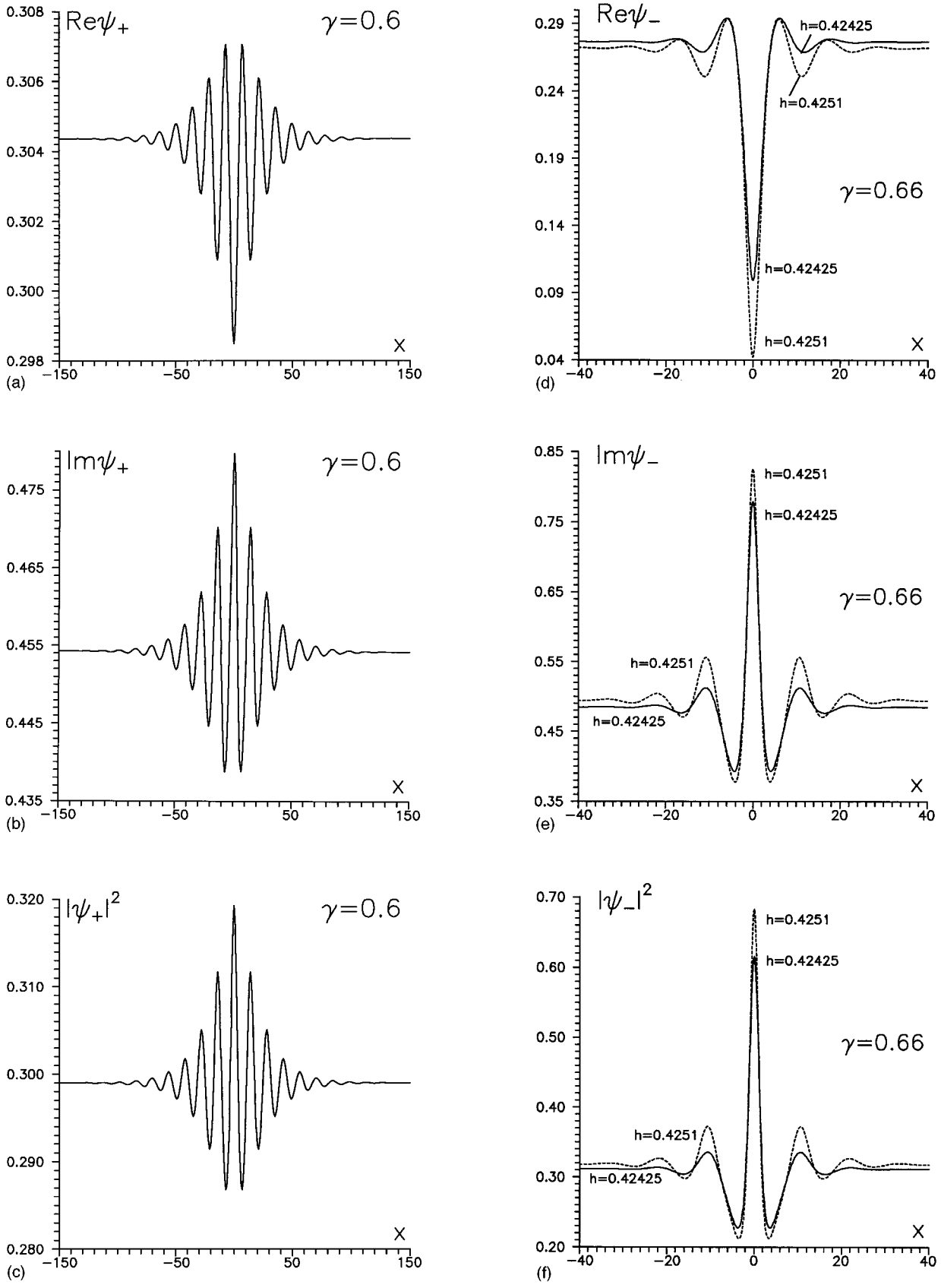

FIG. 12. Solitons in the third region ($\gamma > 1/\sqrt{3}$). (a)–(c) ψ_+ soliton in the neighborhood of the upper boundary of the existence domain. In these plots $\gamma = 0.60$ and $h = 0.394\,92$. (The upper boundary is $h_* = 0.394\,97$.) (d)–(f) ψ_- soliton for $\gamma = 0.66$. Solid line, solution at the threshold $h = h_{\text{thr}} = 0.424\,25$; dashed line, soliton near the upper boundary, $h = 0.4251$. For this γ the value of h_* is 0.4265; however, no ψ_- solitons with $h > 0.4259$ were found.

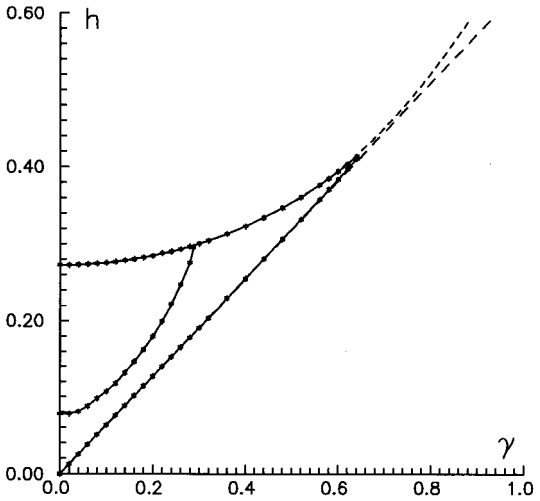

FIG. 13. Existence and stability chart for the soliton solutions of the externally driven, damped NLS. The upper and lower solid lines show the upper and lower boundaries of the solitons' existence domain. The middle solid line is the line of the Hopf bifurcation; above this line the soliton ψ_- is unstable. The upper dashed line is given by Eq. (27) and demarcates the boundary of stability of the flat-locked solution; the lower dashed line is the straight line $h=(2/\pi)\gamma$. Below $\gamma\sim 0.66$, these dashed lines are graphically indistinguishable from the soliton's existence boundaries. They *do not* completely coincide, however (see the text).

$$\nu=\begin{cases}\sqrt{(1-2|\psi_0|^2)(6|\psi_0|^2-1)}, & |\psi_0|^2<1/4\\ 2|\psi_0|^2, & |\psi_0|^2>1/4.\end{cases}$$

Discrete eigenvalues can be complex and real. If μ is an eigenvalue with the eigenfunction $z(x)$, its complex conjugate μ^* is also an eigenvalue with eigenfunction $z^*(x)$. This follows simply from the fact that H is an operator with real coefficients. A less trivial observation is that $(-\mu^*)$ will be an eigenvalue as well; the proof of the latter is relegated to the Appendix.

Thus real eigenvalues of $J^{-1}H$ will always appear in pairs μ and $-\mu$; complex eigenvalues will occur in quadruplets: μ, $-\mu$, μ^*, and $-\mu^*$. For any values of h and γ, the operator $J^{-1}H$ has two discrete eigenvalues: γ and $-\gamma$. (This is true for both ψ_- and ψ_+ solitons.) The eigenvalue $\mu=\gamma$ results from the translational invariance. The corresponding exponent λ in Eq. (20) is equal to zero; the corresponding eigenfunction $z(x)$ is given by

$$z(x)=\frac{d}{dx}\begin{pmatrix}\mathrm{Re}\,\psi_\pm(x)\\ \mathrm{Im}\,\psi_\pm(x)\end{pmatrix}.$$

The negative eigenvalue $\mu=-\gamma$ arises due to the symmetry $\mu\to-\mu$ discussed above.

TABLE I. Numerically calculated upper boundary of the existence domain for the ψ_- soliton. Here ρ_1 denotes the value of $|\psi_0|^2$ for which the ψ_- soliton still exists; h_1 is the corresponding h: $h_1=h(\rho_1)$. Next, ρ_2 is the lowest value of $|\psi_0|^2$ for which Newtonian iterations did not converge and we were unable to find the ψ_- soliton. h_2 is the corresponding h: $h_2=h(\rho_2)$. The actual upper boundary lies somewhere between h_1 and h_2.

γ	$\gamma/2$	ρ_1	ρ_2	h_1	h_2
0.52	0.26	0.254	0.255	0.360 79	0.360 80
0.54	0.27	0.262	0.263	0.368 46	0.368 48
0.56	0.28	0.269	0.270	0.376 53	0.376 57
0.60	0.30	0.298	0.299	0.394 88	0.394 92
0.64	0.32	0.307	0.308	0.414 12	0.414 21
0.66	0.33	0.324	0.325	0.425 85	0.425 86

B. Numerical solution of the eigenvalue problem

We define a grid with spacing $\Delta x=L/(N+1)$:

$$x_n=-\frac{L}{2}+n\Delta x,\quad n=1,2,\ldots,N,$$

with $x_0=-L/2$ and $x_{N+1}=L/2$, and introduce real f_n, g_n:

$$\delta\psi(x_n,t)=(f_n+ig_n)e^{(\mu-\gamma)t}.$$

Approximating the derivatives by second-order finite differences, we reduce the differential eigenvalue problem (21) to a matrix eigenvalue problem of the form

$$\mathbf{Hz}=\mu\mathbf{Jz}. \tag{50}$$

Here $\mathbf{z}$ is a $2N$-component vector

$$\mathbf{z}=\begin{pmatrix}f_1\\ \vdots\\ f_N\\ g_1\\ \vdots\\ g_N\end{pmatrix}$$

and $\mathbf{H}$ and $\mathbf{J}$ are $(2N\times 2N)$ block matrices

$$\mathbf{H}=\begin{pmatrix}-D^2+u & w\\ w & -D^2+v\end{pmatrix},$$

$$\mathbf{J}=\begin{pmatrix}0 & -I\\ I & 0\end{pmatrix}.$$

The entries of the $N\times N$ blocks u, v, w, and I are given by

$$u_{mn}=\{1-2(3\psi_R^2+\psi_I^2)|_{x=x_n}\}\delta_{mn},$$

$$v_{mn}=\{1-2(3\psi_I^2+\psi_R^2)|_{x=x_n}\}\delta_{mn},$$

$$w_{mn}=-4\psi_R\psi_{I|_{x=x_n}}\delta_{mn},$$

$$I_{mn}=\delta_{mn},\quad m,n=1,2,\ldots,N. \tag{51}$$

Finally, D^2 is an $N\times N$ matrix arising from the discretization of the second derivative

$$-D^2=\frac{1}{(\Delta x)^2}\times\begin{pmatrix} 2 & -1 & 0 & 0 & 0 & \cdots & 0 \\ -1 & 2 & -1 & 0 & 0 & \cdots & 0 \\ 0 & -1 & 2 & -1 & 0 & \cdots & 0 \\ & & & \ddots & & & \\ 0 & \cdots & 0 & -1 & 2 & -1 & 0 \\ 0 & \cdots & 0 & 0 & -1 & 2 & -1 \\ 0 & \cdots & 0 & 0 & 0 & -1 & 2 \end{pmatrix}. \tag{52}$$

Since we are interested in *discrete* eigenvalues, we imposed the Dirichlet boundary conditions, $\delta\psi(\pm L/2)=0$, which translate into

$$f_0=f_{N+1}=g_0=g_{N+1}=0. \tag{53}$$

Equations (53) have been taken into account in deriving Eq. (52).

Having fixed γ, we increased h from $h_{\rm thr}$ to $h=h_+(\gamma)$; results turned out to be qualitatively similar for all $\gamma\lesssim 0.3$. Let us start with the ψ_- solution.

As we have already mentioned, there always is an eigenvalue $\mu_0=\gamma$ (or, equivalently, there always is an exponent $\lambda_0=0$) corresponding to the translational symmetry. When $h=h_{\rm thr}$, we have a turning point and, consequently, there is *one more* zero exponent $\lambda_1=0$. That is, at $h=h_{\rm thr}$ we have two pairs of discrete eigenvalues: the translational eigenvalue $\mu_0=\gamma$ and its negative $\tilde{\mu}_0=-\gamma$ (we shall disregard these two eigenvalues in what follows), and the turning point eigenvalue $\mu_1=\gamma$ and its negative $\tilde{\mu}_1=-\gamma$.

As we increase h, the eigenvalues μ_1 and $-\mu_1$ approach each other along the real axis, and coalesce at the origin. Then μ_1 passes on to the positive imaginary axis, and $-\mu_1$ to the negative imaginary axis, and the separation between them increases. As h is increased further, another pair of pure imaginary eigenvalues μ_2 and $-\mu_2$ detaches from the continuum. (We recall that the continuous spectrum occupies the imaginary axis outside the gap $-\omega_0<\mathrm{Im}\mu<\omega_0$.) Subsequently, μ_1 coalesces with μ_2, $-\mu_1$ with $-\mu_2$, and all four eigenvalues move away from the imaginary axis. We end up with a quadruplet μ, μ^*, $-\mu$, and $-\mu^*$.

On further increasing h, the real part of μ and μ^* grows and, at a certain $h=h_{\rm Hopf}$, becomes equal to γ. This is a point of the Hopf bifurcation; for $h>h_{\rm Hopf}$, the soliton ψ_- is unstable.

The above scenario is almost coincident with the scenario described in [15]; there is just one distinction. Terrones *et al.* observed what they called the stability windows: after the first Hopf bifurcation, the pair of complex-conjugate eigenvalues μ and μ^* crossed back into the stable half plane $\mathrm{Re}\mu<\gamma$ and then returned to the unstable region $\mathrm{Re}\mu>\gamma$ again. On the contrary, no stability windows were observed in our calculations. (This contradiction is to be rectified below.) After the pair of complex-conjugate eigenvalues have crossed into the unstable half plane, their real parts were monotonically growing.

Curiously enough, as h approaches the upper boundary of the domain of existence ($h\to h_+$) the limit value of $\mathrm{Re}\mu$ is almost independent of γ. More precisely, as $h\to h_+(\gamma)$, the real part of μ tends to approximately 0.3. This observation provides a simple estimate for the value of γ above which no Hopf bifurcations may occur. Indeed, for $\gamma>0.3$, $\mathrm{Re}\mu$ cannot exceed γ and so the ψ_- soliton is stable for all h (see the stability chart Fig. 13).

Now we turn to the ψ_+ soliton. As we have already mentioned, at $h=h_{\rm thr}$ (the turning point where ψ_+ and ψ_- merge) there is a nontranslational eigenvalue $\mu=\gamma$. (There is also its negative partner $\tilde{\mu}=-\gamma$, but we are concentrating on the positive eigenvalue.) As h is increased, this real eigenvalue grows beyond γ, reaches a maximum, and then starts decreasing. This evolution is accompanied by the restructuring of the continuous spectrum. As $|\psi_0|^2$ grows beyond 1/6, the gap $-\omega_0<\mathrm{Im}\mu<\omega_0$ in the continuous spectrum closes. Now the continuous spectrum fills in the entire imaginary axis and, on the top of this, the region $-\nu<\mathrm{Re}\mu<\nu$ on the real axis. The value ν is smaller than γ but grows as h is increased. Finally, when h reaches the upper boundary of the domain of existence [$h_+(\gamma)$ for $\gamma<1/2$ and $h_*(\gamma)$ for $\gamma>1/2$, respectively], ν reaches γ. This is a point of bifurcation where the soliton ψ_+ merges with the flat solution. Accordingly, at this h the real eigenvalue μ reaches γ from above and immerses into the continuous spectrum.

C. Stability windows

It is important to trace the origin of the contradiction between our results and conclusions of Ref. [15], in particular to clarify the issue of stability windows. We shall demonstrate that the contradiction stems simply from the fact that Terrones *et al.* consider much shorter intervals L.

Terrones *et al.* impose periodic boundary conditions on perturbations $\delta\psi(x)$,

$$\delta\psi(-L/2)=\delta\psi(L/2),\quad \delta\psi_x(-L/2)=\delta\psi_x(L/2), \tag{54}$$

whereas in Sec. IV B we worked with the Dirichlet conditions

$$\delta\psi(\pm L/2)=0. \tag{55}$$

In order to eliminate a possible effect of the boundary conditions, we have now replaced our vanishing conditions (55) by the periodic conditions (54). In terms of the discretized eigenfunctions, this amounts to replacing Eqs. (53) by

$$f_0=f_N,\ f_{N+1}=f_1,\quad g_0=g_N,\quad g_{N+1}=g_1. \tag{56}$$

The only consequence of this substitution is that the matrix $-D^2$ [Eq. (52)] is replaced by

$$-\widetilde{D}^2=\frac{1}{(\Delta x)^2}\times\begin{pmatrix} 2 & -1 & 0 & 0 & 0 & \cdots & 0 & -1 \\ -1 & 2 & -1 & 0 & 0 & \cdots & 0 & 0 \\ 0 & -1 & 2 & -1 & 0 & \cdots & 0 & 0 \\ & & & \ddots & & & & \\ 0 & 0 & \cdots & 0 & -1 & 2 & -1 & 0 \\ 0 & 0 & \cdots & 0 & 0 & -1 & 2 & -1 \\ -1 & 0 & \cdots & 0 & 0 & 0 & -1 & 2 \end{pmatrix}. \tag{57}$$

The D^2 and $\widetilde{D}^2$ are only different in their lower left and upper right corner entries.

In Eqs. (51), $\psi_-=\psi_R+i\psi_I$ satisfies its standard ''open end'' boundary conditions $\psi_x(\pm L/2)=0$. Since $\psi_-(x)$ is an even function, these boundary conditions are equivalent to periodic conditions $\psi(-L/2)=\psi(L/2)$, $\psi_x(-L/2)=\psi_x(L/2)$. Thus we examine the stability of exactly the same solution as Terrones *et al.*

Those authors report the occurrence of the stability windows for the following two sets of the sine-Gordon parameters: $L_{\mathrm{SG}}=24$, $\alpha=0.04$, (a) $\omega=0.87$, and (b) $\omega=0.90$. Using Eqs. (7)–(9), one gets the corresponding NLS values

$$\text{(a)}\quad L_{\mathrm{NLS}}=12.2376,\quad \gamma=0.1538,\quad h=\frac{\Gamma}{0.5303};$$

$$\text{(b)}\quad L_{\mathrm{NLS}}=10.7331,\quad \gamma=0.2000,\quad h=\frac{\Gamma}{0.3578}.$$

(Here Γ and h are the sine-Gordon and NLS driving strengths, respectively.)

We have calculated the eigenvalues μ for the first set of control parameters, i.e., we took $L=12.2376$, fixed $\gamma=0.1538$, and varied h. The growth rate $\mathrm{Re}\lambda=\mathrm{Re}\mu-\gamma$ is plotted in Fig. 14(a) (solid line). Clearly seen is the region where $\mathrm{Re}\lambda<0$, the stability window. The values of h at which the solution restabilizes exactly correspond to those given in Ref. [15].

It is appropriate to emphasize here that although we have analyzed exactly the same eigenvalue problem as Terrones *et al.*, their numerical approach was totally different. Those authors worked with the (truncated) Fourier expansion, while we use the finite-difference approximation. Consequently, the exact correspondence of our results with results of [15] rules out any chance of numerical error.

We next increased the length of the integration interval (from $L=12.238$ to $L=15$) keeping γ fixed. Surprisingly, this minor change resulted in that the stability window has closed [the short-dashed curve in Fig. 14(a)]. On further increasing L, the stability interval did not reappear. [The long-dashed line in Fig. 14(a) shows the growth rate for $L=60$.]

For the sake of comparison we repeated the calculation for the same values of L and γ, but with the Dirichlet boundary conditions on eigenfunctions Eq. (55). Similarly to the periodic case, the curve $\mathrm{Re}\lambda(h)$ changes substantially as L is increased from 12.238 to 15, but on further increases, results settle down [see Fig. 14(b)]. For sufficiently large intervals ($L=60$ in our case) discrete eigenvalues are insensitive to the type of the boundary conditions.

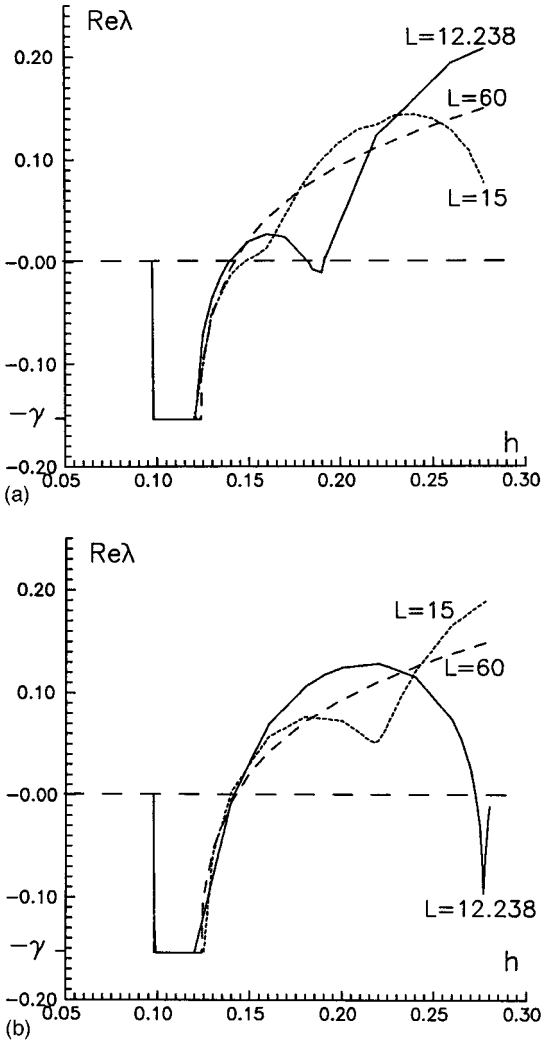

FIG. 14. Maximum growth rate $\mathrm{Re}\lambda$ ($=\mathrm{Re}\mu-\gamma$) as a function of h for $\gamma=0.1538$. Solid line, $L=12.238$; short-dashed line, $L=15$; long-dashed line, $L=60$. (a) Periodic boundary conditions for eigenfunctions; (b) vanishing boundary conditions. The horizontal straight-line portions of the curves (where $\mathrm{Re}\lambda=-\gamma$) correspond to pure imaginary eigenvalues μ. For $h\lesssim 0.12$ all three curves practically coincide.

Concluding, we may claim that stability windows may occur only for sufficiently small interval lengths. This phenomenon is apparently of the same origin as the stabilization of the upper branch of the flat solution when the interval is made sufficiently short [15]. The instability is caused by long-wavelength perturbations that cannot arise on short intervals.

V. CONCLUDING REMARKS AND OPEN PROBLEMS

The principal result of this study is the chart of phase-locked attractors on the (h,γ) plane [Fig. 13]. This chart

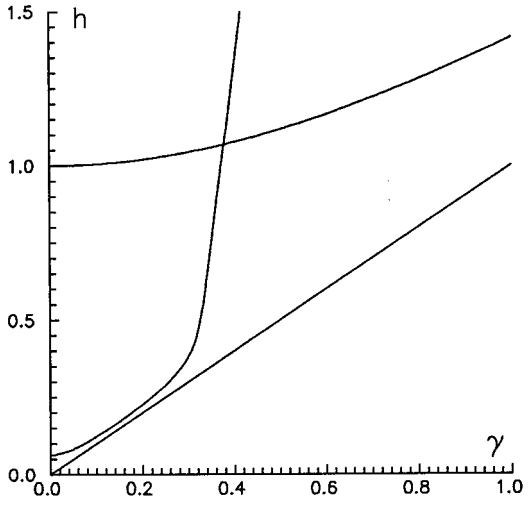

FIG. 15. Existence and stability chart for the *parametrically* driven NLS equation (3) as from Ref. [16]. (The driving frequency Ω has been normalized to unity.) The structure of the chart is very similar to Fig. 13. The lowest line is the lower boundary of the soliton existence domain; in the parametric case $h_{\rm thr}=\gamma$. The uppermost curve is given by $h=\sqrt{1+\gamma^2}$ and plays the role of the upper boundary of the existence domain. Although the soliton does exist above this line, it is unstable there, together with the zero solution, against continuous spectrum excitations. Finally, the middle line is the curve of the Hopf bifurcation; on crossing this line the stationary soliton loses its stability to a temporally periodic solution. The structure of the unstable domain (above the Hopf bifurcation line) is shown in Fig. 16.

comprises the existence and stability domains of the spatially homogeneous solution and two coexisting solitons ψ_+ and ψ_-. While ψ_+ is unstable for all h and γ, stability properties of ψ_- depend on whether γ is greater or smaller than $\gamma_{\rm cr}$, where $\gamma_{\rm cr}\approx 0.3$. When $\gamma>\gamma_{\rm cr}$, the ψ_- soliton is stable for all h; when $\gamma<\gamma_{\rm cr}$, the increasing of h results in ψ_- losing its stability via a Hopf bifurcation.

The classification of the phase-locked attractors on the (h,γ) plane is the first step towards the construction of the *complete* attractor chart. Our next step will be to study nonlinear structures in the region where the ψ_- soliton is unstable, i.e., above the Hopf bifurcation curve. Here some guidance can be gained from the analysis of a twin problem, namely, the *parametrically* driven NLS equation [16]. Figure 15 displays the existence and stability chart for the parametrically driven damped soliton; it bears a striking similarity to our chart for the externally driven NLS (Fig. 13). It is therefore natural to expect that the structure of the attractor chart above the Hopf bifurcatrion curve will also be similar. Figure 16 is the complete chart of attractors for the parametrically driven case that we reproduce from Ref. [17]. Seen are two lines of different types of transition to chaos, period doubling and quasiperiodic, meeting at a ''tricritical point.'' It is tempting to expect that the topography of attractors of the externally driven NLS equation will be qualitatively similar. Numerical simulations of Eq. (2) available for several γ [6–12] do not contradict this hypothesis.

It is pertinent to emphasize two main distinctions of our study from the work of Terrones *et al.* [15]. First, those authors analyze solutions on a *finite* interval $(-L/2,L/2)$ with periodic boundary conditions, whereas the present article deals with *infinite* intervals. In their numerical calculations, Terrones *et al*. focus on rather short intervals $L\sim$ 10–15, for which the effect of the boundaries cannot be neglected. Accordingly, some properties of their *periodic solutions* differ substantially from properties of *solitons* reported in this paper. In particular, as we have observed for $\gamma=0.1538$, it is sufficient to increase the interval length from $L\sim 12$ to 15 to see the stability window of the ψ_- solution closing.

Second, the aim of Ref. [15] was to give a theoretical explanation for results of the available numerical simulations; accordingly, the authors of [15] restricted their attention to several specific values of γ. On the contrary, our objective here is to provide a global view: to chart the whole (h,γ) plane according to habitats of various flat and solitonic attractors.

As we mentioned on several occassions, there are three characteristic regions of the dissipation coefficient: $\gamma<1/2$, $1/2<\gamma<1/\sqrt{3}$, and $\gamma>1/\sqrt{3}$. The existence and stability properties of flat and solitonic solutions depend on which region we are in. Results of Ref. [15] are confined to the region $\gamma<1/2$.

One may argue that in applications, the damping and driving are weak, so does it really make sense to consider large values of h and γ? The answer is that, apart from their own role in plasma, optics and other applications, the damped driven NLS solitons describe small amplitude breathers of the damped driven sine-Gordon equation (1). The damping and driving coefficients of the two equations are related by Eq. (7):

$$\gamma=\frac{\alpha}{\varepsilon^2},\quad h=\frac{\Gamma}{4\varepsilon^3}, \tag{58}$$

where the detuning

$$\varepsilon=\sqrt{2(1-\omega)} \tag{59}$$

acts as a small parameter. Consequently, even if the sine-Gordon dissipation coefficient α and driving strength Γ are small, their NLS counterparts may be quite large.

It is instructive to make a link to results of *direct* computer simulations of the sine-Gordon and NLS equations available in literature.

Nozaki and Bekki [6] simulated the NLS equation (2) with $\gamma=0.1$ on a relatively large interval $L=50$ and found that the soliton becomes unstable for $h>0.11$. This is in perfect agreement with the value $h_{\rm Hopf}=0.11$, which we have obtained in the numerical solution of the eigenvalue problem (Sec. IV B).

In their computer experiments with the sine-Gordon (SG) equation (1), Bishop *et al.* [8] set $\alpha=0.04$, $L_{\rm SG}=24$, and produced an attractor chart on the (Γ,ω) plane for $0\leqslant\Gamma\leqslant 0.19$ and $0.82\leqslant\omega\leqslant 0.94$. In terms of the NLS control parameters, these simulations correspond to $0.11\leqslant\gamma\leqslant 0.33$.

Eliminating ε between (58) and (59), we have

$$\omega=1-\frac{1}{2}\,\frac{\alpha}{\gamma}. \tag{60}$$

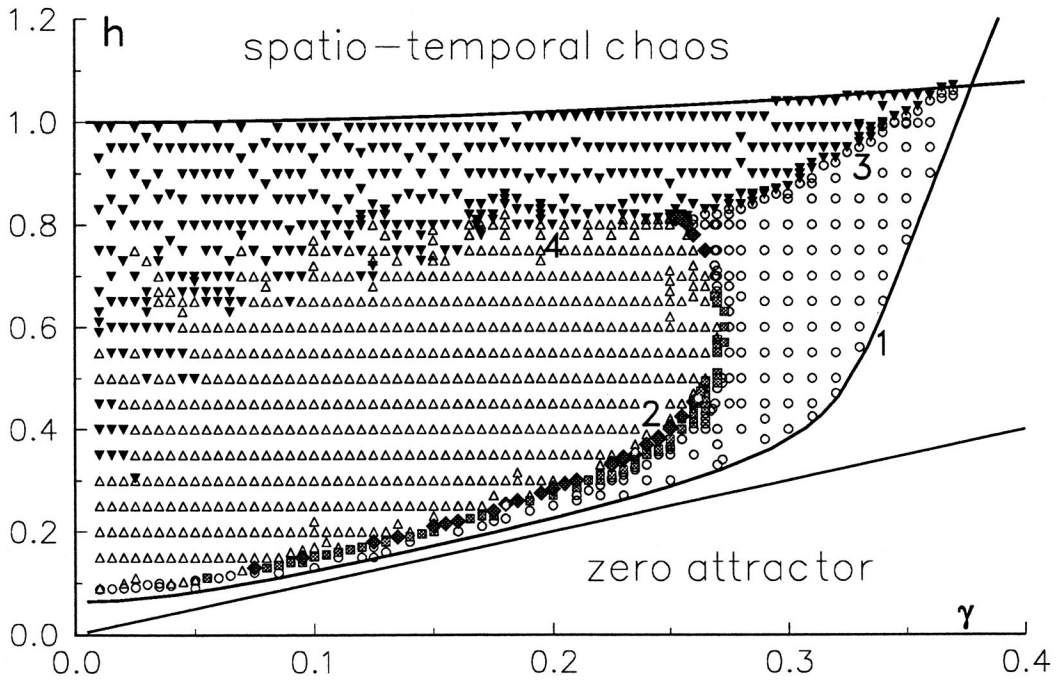

FIG. 16. Attractor chart of the parametrically driven, damped NLS equation from Ref. [17]. Below the straight line $h=\gamma$ (the lowest line in this plot) the only attractor is the trivial one $\psi\equiv 0$. Above the line $h=\sqrt{1+\gamma^2}$ (the uppermost line in the picture) the trivial solution is unstable with respect to continuous spectrum waves. Line 1 is the Hopf bifurcation curve; stable stationary solitons exist below and to the right of this curve. On crossing curve 1, stationary attractors are replaced by temporally periodic solitons (marked by empty circles). These can subsequently bifurcate into double-periodic, four-, and eight-periodic solitons (shadowed boxes). Small white blobs and shadowed diamonds represent more complicated attractors (periods 6, 7, 10, and temporally chaotic). Above curve 2, empty triangles mark the area where only the trivial attractor exists; black triangles stand for spatiotemporal chaotic states. An alternative scenario of the transition to chaos occurs on crossing line 3; here the periodic soliton is replaced by the spatiotemporal chaotic attractor without any intermediate period doubling. The two scenarios ''meet'' at a tricritical point $h=0.81, \gamma=0.25$. Finally, in the region above the line $h=\sqrt{1+\gamma^2}$ and to the left of the Hopf bifurcation curve 1, the instability of the zero solution develops into spatiotemporal chaos.

Thus, for the fixed SG damping α, the frequency ω is completely specified by the NLS damping γ; fixing ω is equivalent to fixing γ. The SG forcing Γ is then proportional to the NLS forcing h,

$$\Gamma=4\left(\frac{\alpha}{\gamma}\right)^{3/2}h. \tag{61}$$

Assume that the NLS damping coefficient γ is fixed and forcing h varied. Figure 13 shows that the larger γ is, the smaller the range of h for which the NLS soliton is unstable. Translating to the sine-Gordon variables, Eqs. (60) and (61) imply that for fixed α and ω there is an interval of Γ's where the breather is unstable; this interval should shrink as ω is increased. This was indeed observed in [8] for not very small detunings $\varepsilon\geqslant 0.45$ (that is, for $\omega\leqslant 0.9$); see Fig. 1 in [8]. For smaller detunings ε (larger ω) results start to deviate. This may be attributed to the fact that the NLS interval corresponding to $L_{\mathrm{SG}}=24$ becomes very short ($L_{\mathrm{NLS}}=\varepsilon L_{\mathrm{SG}}<10.8$).

Taki *et al.* [10] studied the sine-Gordon equation with $\alpha=0.004$, $L_{\mathrm{SG}}=80$, $\omega=0.98$, and $0.0585\leqslant\Gamma\leqslant 0.116$. This corresponds to $\gamma=0.1$ and $L_{\mathrm{NLS}}=16$. For $\Gamma=0.0038$, the breather lost its stability via a Hopf bifurcation. The corresponding h is equal to 0.12, which is close to our $h_{\mathrm{Hopf}}=0.11$; the difference should be attributed to the smallness of the interval.

Spatschek *et al.* [11] simulated the NLS equation (2) on an interval $L=40$ for a variety of h and γ ($\gamma<0.25$). Their experimental points fit very well into the $\gamma<0.25$ portion of our stability chart Fig. 13.

Finally, it has remained unclear what happens to the soliton ψ_- as $|\psi_0|^2\to\gamma/2$ in the region $\gamma>1/2$. As we mentioned in Sec. III D, we were unable to find the solution ψ_- close enough to the value $|\psi_0|^2=\gamma/2$; the Newtonian iterations ceased to converge a certain finite distance away from $\gamma/2$. (This is in a sharp contrast to the case of the ψ_+ solitons, which turned out to exist arbitrarily close to the value $|\psi_0|^2=\gamma/2$.) It would be interesting to understand whether the upper boundary of the existence domain of the ψ_- soliton is indeed different from $|\psi_0|^2=\gamma/2$ or this is simply a numerical effect caused by an anomalously small radius of convergence of Newton's method in the neighborhood of the boundary.

ACKNOWLEDGMENTS

We would like to thank M. M. Bogdan, in conversations with whom the idea of this work was borne and shaped. We are grateful to R. Cross, V. B. Priezzhev, I. V. Puzynin, B. D. Reddy, N. Robertson, and A. Rynhoud for useful discussions and M. Bondila for her computational assistance. This research was supported by the FRD of South Africa, University Research Council of UCT and Laboratory for Comput-

ing Techniques and Automation of JINR. The work of Yu. S. Smirnov was also supported by the Russian Foundation of Fundamental Research (Grant No. 94-01-01119).

APPENDIX

The aim of this appendix is to show that if μ is a discrete eigenvalue of the operator $J^{-1}H$ [Eq. (21)], $-\mu^*$ is an eigenvalue as well. To this end we define an auxiliary operator A_μ,

$$A_\mu = H - \mu J,$$

where μ is a complex parameter and J is given by Eq. (18). If η is an eigenvalue of A_μ,

$$A_\mu z(x) = \eta z(x),$$

η^* will be an eigenvalue of the Hermitian-conjugate operator $A_\mu^\dagger$ where

$$A_\mu^\dagger = H - \mu^* J^\dagger = H + \mu^* J = A_{-\mu^*}.$$

(Notice that taking the Hermitian conjugate amounts to replacing μ by $-\mu^*$.) Assume now that $z_0(x)$ is an eigenfunction of the operator $J^{-1}H$ corresponding to the eigenvalue μ_0:

$$Hz_0(x) = \mu_0 J z_0(x).$$

This $z_0(x)$ is, at the same time, an eigenfunction of the operator A_μ pertaining to the parameter value $\mu = \mu_0$ and eigenvalue $\eta = 0$:

$$A_{\mu_0} z_0(x) = (H - \mu_0 J) z_0(x) = 0.$$

The conjugate operator $A_{\mu_0}^\dagger$ $(= A_{-\mu_0^*})$ will also have an eigenvalue $\eta^* = 0$; this implies that $-\mu_0^*$ is an eigenvalue of $J^{-1}H$. Q.E.D.

There is one point in the above proof that requires a word of caution. If η is an eigenvalue of A, a non-Hermitian operator in the Hilbert space, the conjugate operator $A^\dagger$ does not, in general, have to have an eigenvalue η^*. Consider, for example, a shift operator T defined on infinite sequences $\mathbf{x} = (x_1, x_2, \dots)$:

$$T(x_1, x_2, x_3, \dots) = (x_2, x_3, x_4, \dots). \tag{A1}$$

It is easy to see that $\eta = 0$ is an eigenvalue of T, with an eigenvector $(1,0,0,\dots)$. However, the conjugate operator $T^\dagger$ does not have a zero eigenvalue. This follows from the fact that the kernel space of $T^\dagger$ (i.e., the space of all $\mathbf{x}$ such that $T^\dagger \mathbf{x} = 0$) is given by $\mathcal{R}(T)^\perp$, the orthogonal complement of the range of T. Since the range of the shift operator (A2) obviously coincides with the entire space, $\mathcal{R}(T)^\perp$ consists only of the zero element and so $T^\dagger$ has no zero eigenvalues.

Fortunately, this situation does not arise for discrete eigenvalues of differential operators (whose eigenfunctions are smooth and exponentially decaying at infinities). The reason is that these eigenvalues can be approximated by eigenvalues of finite-dimensional matrices. For instance, one can approximate derivatives by finite differences (as we do in Sec. IV B) or use a truncated expansion over some complete set of functions (which is the approach of Ref. [15]). In any case, sending $N \to \infty$, one of the eigenvalues of the $N \times N$ matrix A_N will approach the discrete eigenvalue of the differential operator A: $\eta_N \to \eta$. On the other hand, if η_N is an eigenvalue of the matrix A_N, the Hermitian-conjugate matrix $A_N^\dagger$ will have an eigenvalue η_N^*. When $N \to \infty$, the sequence η_N^* converges to a discrete eigenvalue of the Hermitian-conjugate operator $A^\dagger$, which is therefore equal to η^*.

Returning to the shift operator Eq. (A1), notice that its zero eigenvalue *cannot* be approximated by a sequence of finite-dimensional matrix eigenvalues. In particular, if we attempt to use a finite-dimensional shift operator with periodic boundary conditions

$$T_N(x_1, x_2, \dots, x_N) = (x_2, x_3, \dots, x_N, x_1),$$

we will immediately find that eigenvalues of the latter are given by $\exp(2\pi i n/N)$, $n = 0,1,\dots,N-1$. None of these tend to zero as $N \to \infty$.

[1] D. J. Kaup and A. C. Newell, Proc. R. Soc. London Ser. A **361**, 413 (1978).
[2] D. J. Kaup and A. C. Newell, Phys. Rev. B **18**, 5162 (1978).
[3] J. C. Eilbeck, P. S. Lomdahl, and A. C. Newell, Phys. Lett. **87A**, 1 (1981); D. Bennett, A. R. Bishop, and S. E. Trullinger, Z. Phys. B **47**, 265 (1982); A. R. Bishop, K. Fisser, P. S. Lomdahl, W. C. Kerr, M. B. Williams, and S. E. Trullinger, Phys. Rev. Lett. **50**, 1095 (1983); A. R. Bishop, K. Fesser, P. S. Lomdahl, and S. E. Trullinger, Physica D **7**, 259 (1983).
[4] E. A. Overman, D. W. McLaughlin, and A. R. Bishop, Physica D **19**, 1 (1986).
[5] K. Nozaki and N. Bekki, Phys. Rev. Lett. **50**, 1226 (1983); Phys. Lett. **102A**, 383 (1984).
[6] K. Nozaki and N. Bekki, J. Phys. Soc. Jpn. **54**, 2363 (1985).
[7] K. Nozaki and N. Bekki, Physica D **21**, 381 (1986).
[8] A. R. Bishop, M. G. Forest, D. W. McLaughlin, and E. A. Overman, Physica D **23**, 293 (1986).
[9] A. Mazor, A. R. Bishop, and D. W. McLaughlin, Phys. Lett. A **119**, 273 (1986); A. Mazor and A. R. Bishop, Physica D **27**, 269 (1987).
[10] M. Taki, K. H. Spatschek, J. C. Fernandez, R. Grauer, and G. Reinisch, Physica D **40**, 65 (1989).
[11] K. H. Spatschek, H. Pietsch, E. W. Laedke, and Th. Eickermann, in *Singular Behaviour and Nonlinear Dynamics*, edited by T. Bountis and St. Pnevmatikos (World Scientific, Singapore, 1989).
[12] R. Grauer and B. Birnir, Physica D **56**, 165 (1992).
[13] Th. Eickermann, R. Grauer, and K. H. Spatschek, Phys. Lett. A **198**, 383 (1995).

[14] I. V. Barashenkov, M. M. Bogdan, and T. Zhanlav, in *Nonlinear World*, Proceedings of the Fourth International Workshop on Nonlinear and Turbulent Processes in Physics, Kiev, 1989, edited by V. G. Bar'yakhtar *et al.* (World Scientific, Singapore, 1990), p. 3.

[15] G. Terrones, D. W. McLaughlin, E. A. Overman, and A. J. Pearlstein, SIAM J. Appl. Math. **50**, 791 (1990).

[16] I. V. Barashenkov, M. M. Bogdan, and V. I. Korobov, Europhys. Lett. **15**, 113 (1991).

[17] M. Bondila, I. V. Barashenkov, and M. M. Bogdan, Physica D **87**, 314 (1995).

[18] The formation of soliton bound states was studied within the perturbative framework; see B. A. Malomed, Phys. Rev. A **44**, 6954 (1991); **45**, 8321 (1992); Phys. Rev. E **47**, 2874 (1993); D. Cai, A. R. Bishop, N. Grønbech-Jensen, and B. A. Malomed, *ibid.* **49**, 1677 (1994). Two underlying assumptions were that (i) h and γ are small and (ii) the separation between solitons is large. The possibility of bound states to occur for *finite* h and γ is an open question, however, as well as whether strongly overlapping solitons may bind together.

[19] The continuous analog of Newton's method (also known as the variable iteration step Newton method) was formulated by M. K. Gavurin, Izv. Vuzov Mat. **5-6**, 18 (1958). For reviews see, e.g., E. P. Zhidkov, G. I. Makarenko, and I. V. Puzynin, Fiz. Elem. Chastits At. Yadra **4**, 127 (1973) [Sov. J. Part. Nucl. **4**, 53 (1973)]; L. Bracci and G. Fiorentini, Phys. Rep. **86**, 170 (1982). Recent advances are discussed by T. Zhanlav and I.V. Puzynin, Comp. Math. Math. Phys. **32**, 729 (1992); **32**, 1 (1993); **34**, 143 (1994). The procedure of the optimal iteration step choice that we follow was suggested by V. V. Ermakov and N. N. Kalitkin, Zh. Vych. Mat. Mat. Fiz. **21**, 491 (1981).